Absolute Radiation Measurements in Earth and Mars Entry Conditions

Brett A. Cruden
ERC Inc. at NASA Ames
NASA Ames Research Center, MS 230-2
Moffett Field, CA 94035
USA

Brett.A.Cruden@nasa.gov

ABSTRACT

This paper reports on the measurement of radiative heating for shock heated flows which simulate conditions for Mars and Earth entries. Radiation measurements are made in NASA Ames' Electric Arc Shock Tube at velocities from 3-15 km/s in mixtures of N_2/O_2 and $CO_2/N_2/Ar$. The technique and limitations of the measurement are summarized in some detail. The absolute measurements will be discussed in regards to spectral features, radiative magnitude and spatiotemporal trends. Via analysis of spectra it is possible to extract properties such as electron density, and rotational, vibrational and electronic temperatures. Relaxation behind the shock is analyzed to determine how these properties relax to equilibrium and are used to validate and refine kinetic models. It is found that, for some conditions, some of these values diverge from non-equilibrium indicating a lack of similarity between the shock tube and free flight conditions. Possible reasons for this are discussed.

1.0   INTRODUCTION

For spacecraft entering planetary atmospheres or returning to Earth's atmosphere, the significant velocities required result in a rapid conversion of kinetic energy into thermochemical energy of the atmospheric gas. This shock heated gas may reach temperatures of thousands to tens of thousands of degrees, resulting in decomposition and ionization of the gas. This high gas enthalpy is imparted to the entering spacecraft and must be buffered against through the use of thermal protection systems (TPS). There are chiefly two mechanisms of heating in planetary re-entry: convection, whereby the energy is transferred to the heat shield via the flow of the gas, and radiation, where excited states of the gas transition and emit electromagnetic radiation in all directions. The radiation that strikes the TPS is then (mostly) absorbed, thereby radiatively heating the surface. The radiative magnitude is typically assumed unimportant at low velocity (i.e. < 10 km/s), but scales in an exponential-type fashion with velocity (scaling laws of v^8 are often quoted) so can become significant or even dominant for high velocity entries. However, the radiative environment is unique to specific gas compositions and flow geometries, so must be independently assessed for different entry scenarios.

In recent years, the Electric Arc Shock Tube (EAST) facility at NASA Ames has been employed for the purpose of obtaining validation data for radiative heating on planetary entry.[1-12] The shock tube produces high velocity flows in gases of known composition and densities relevant to various atmospheric entries. This is achieved by creating a sudden pressure discontinuity which moves hypersonically into the gas in front of it, in the form of a normal shock wave. Because of the short time scales involved, the discontinuity does not mix into its neighboring gas but rather compresses the gas as it moves forward, much like a spacecraft will do to the atmosphere during planetary entry. This shock wave in the driven gas therefore is assumed to have similarity with the bow shock in an entry scenario. A radiating shock wave can be imaged as it passes through the shock

tube, and separated into different wavelengths via spectroscopic equipment. The spectroscopic imaging of the shock is important as the radiation varies strongly and non-monotonically with wavelength, so the ability to predict and model the radiance is dependent upon knowing the spectral features. For most cases of interest, a significant fraction (approx. half) of the radiance will come from vacuum ultraviolet (100-200 nm) wavelengths. The remainder of radiation typically comes from the ultraviolet through near infrared (200-1200 nm), although in some cases of interest mid-wave infrared radiation (2000-6000 nm) will be dominant.

2.0   METHODOLOGY

The EAST facility, and the measurement methodology, has been described in some detail previously. Enhancements to the facility in a major upgrade in 2008 have also been described.[2] Here we review several of the key details of the facility and provide additional detail regarding the measurement approach.
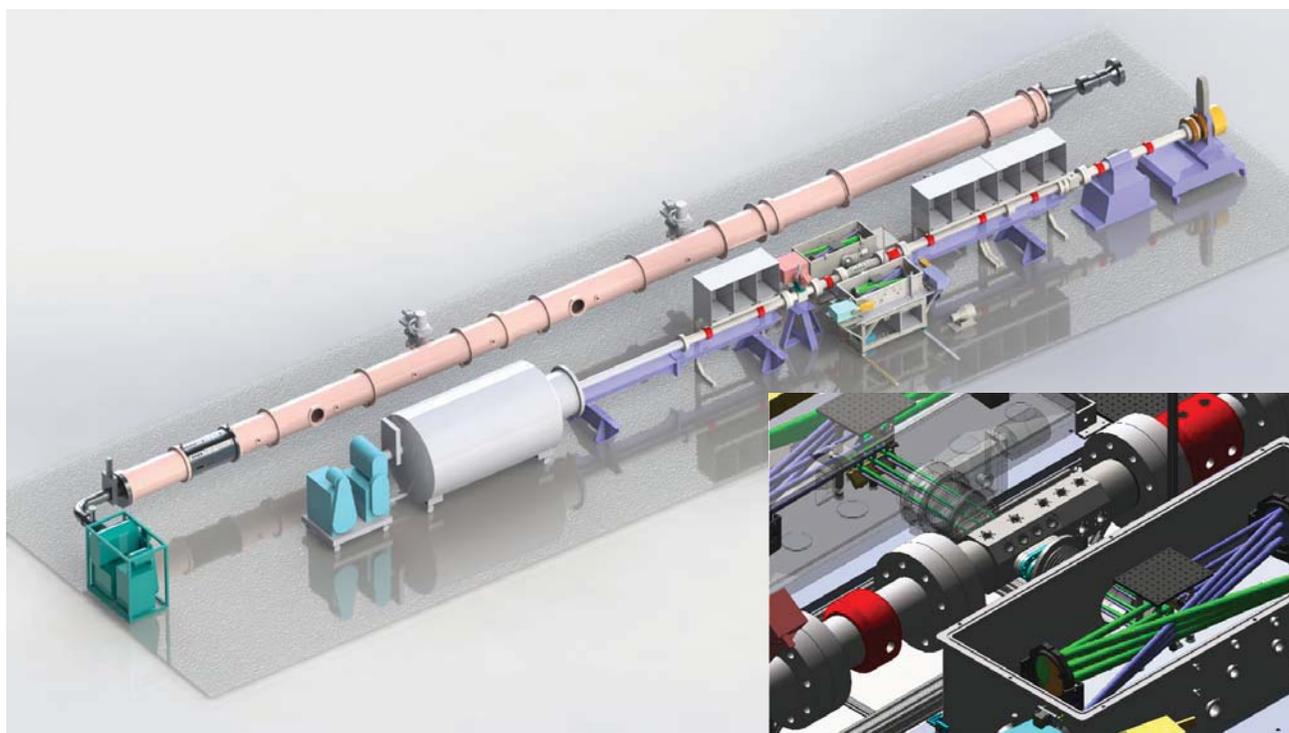
Figure 1. Rendering of the EAST Facility showing both shock tubes. (upper inset) cross-section of driver assembly, (lower inset) close-up of test section and optical boxes.

The EAST facility, shown in Figure 1, consists of two shock tubes and one shared driver system. The driver section (upper insert of Figure 1) is a 1.3L cylindrical-conical section which is separated from the shock tube by a diaphragm of various materials (stainless steel, aluminum and mylar have all been used at different times). The volume of the driver section is primarily defined by a Teflon liner, which insulates the driver gas from its steel housing. For testing, the driver is filled with a driver gas having high speed of sound, such as Hydrogen or Helium, at pressures between 30-200 psi. Some experimentation has been performed with different pressures and gas composition to optimize test time and velocity; however, due to inherent variability in the arc system, the conclusions of these studies are mostly qualitative. At the narrow end of the driver is a copper pin which is attached by a distributor plate and 30 coaxial cables to a 1.3 mF capacitor bank capable of holding up to 1.2 MJ

of energy at voltages of 40 kV. The wide end of the driver cone is 4" in diameter and ends (just prior to the diaphragm) at a ground ring, to which a trigger wire is attached. Two different configurations of the ground ring and trigger wire have been used in recent history. The first consists of a 4" diameter ground ring, concentric with the tube, with the wire coming across the diameter of the tube and then down the center axis in a "T" configuration. The second, "spider" configuration (shown in Figure 1), has a stainless steel cross in the center of the ground ring. The trigger wire is fed through a copper pin at the center of the cross. In both cases, the axial portion of the trigger wire is wound in a spiral so that it may be pulled straight toward the charged pin. When the separation between the pin and the wire is sufficiently small, an arc will jump across the pin and current flows from the pin to the ground electrode. The current will immediately vaporize the trigger wire, at which point an arc attaches from the pin to the grounding ring. The idea with the spider configuration is for the arc to repeatedly attach to the center pin rather than to the side of the tube, thus heating the driver section more uniformly and giving more repeatable shot results with high test times. The first several tests with the spider electrode showed dramatic improvement in test time, however within less than ten tests the driver behavior had returned to a performance level that was not significantly different than that obtained with the "T" configuration. Instantaneous currents measured from the capacitor bank are as high as 1 MA. The capacitor-driver circuit forms an RLC type electrical circuit as evidenced by a damped oscillation of voltage and current over the period of several 100 μs. The arc will heat the driver gas rapidly over tens of microseconds until the diaphragm is either ruptured (by pressure expansion) or vaporized (by high gas temperature), or both. At this point, a pressure discontinuity is created which drives a shock wave down the tube.

The driver assembly can be used interchangeably with either of the two shock tubes by physically moving and attaching the driver assembly to the selected tube. The primary tube in operation (grey tube in Figure 1) is a 4 inch diameter, 15-m long, aluminum tube. The second tube (pink tube in Figure 1), which has been used less extensively, is a 23.75" inner diameter, stainless steel tube that is 23.5 m long. Since the exit diameter of the driver is 4", a short (~2 m) tube section of 4" diameter is attached from the end of the driver to the entry of the 24" tube. A conical section is used to expand the gas out to the full internal diameter at the entry of the 24" tube section. In either case, once the shock wave is launched down the tube, its progress is monitored by a series of pressure sensors (PCB 132A35), fiber-optic coupled photodiodes (Hammamatsu H6780-20) or in-house ionization gauges. These gauges are placed at positions along the tube which are defined by permanent port openings within the tube. The locations of the ports can be seen in the figure at the red rings on the 4" tube or as small circular openings on the 24" tube and 4" test section (lower insert). The sensors detect a sudden discontinuity in the gas phase (be it pressure, light emission or electrical conductivity) which correspond to the arrival of the shock wave. In this manner, the position of the shock as a function of time may be obtained. This is often visualized in the form of an x-t diagram. The derivative of the x-t diagram yields the velocity of the shock wave as a function of location in the tube. The shock will have travelled the length of the tube in less than a millisecond. At the end of the tube, the shock is either expanded into a dump tank (4" tube) or reflected off the tube wall (24" tube), though the intended measurement is already completed by the time this happens.

The primary analysis of the shock is performed in the test section (lower insert of Figure 1), located 7.5 m downstream of the diaphragm in the 4" tube. The test section is more heavily instrumented than the upstream portion of the tube. In this section, time of arrival sensors are placed 3.175 cm apart, giving a much higher resolution velocity measurement. Additionally, a longer (4.75") slot window is present for imaging the shock wave. The long end of the slot window runs along the axis of the tube, allowing the radiation emitted from the shock wave to be observed with spectroscopic instrumentation. A series of 6 mirrors takes the radiance emitted, rotates it 90 degrees and demagnifies it by a factor of about 10. The resulting image is shone upon the slit of a spectrometer. Four different sets of optics, each with its own spectrometer, perform this imaging at four different azimuthal angles, but at the same axial location. The spectrometers disperse the light by wavelength, while retaining its profile along the tube axis. The image, dispersed in wavelength, then falls upon a 2D CCD

array at the spectrometer outlet. The CCDs are electronically shuttered at high speed (sub-µs) to obtain a snapshot of the radiance, which is resolved by position on one axis, and wavelength on the other. The test section in the 24" tube, located approximately 21 m downstream of the diaphragm, is being planned for refurbishment to mimic the features of the section on the 4" tube. The present legacy test section consists solely of two large window openings and two small time of arrival ports through which measurements may be performed.

The four spectrometers are generally chosen to measure different regions of the electromagnetic spectrum. The regions are generally classified as Vacuum Ultraviolet (120-200 nm), Ultraviolet/Visible (200-500 nm), Visible/Near Infrared (500-900 nm), Near Infrared (900-1600 nm) and Mid Wave Infrared (1600-5500 nm). Each of these regions pose different requirements from the standpoint of detectors and instrumentation. Emission in the vacuum ultraviolet is absorbed by ambient oxygen, and therefore requires the entire optical path to be operated under vacuum or nitrogen purge gas. Generally, vacuum is preferred as a nitrogen purge may contain up to 10 ppm of oxygen, while a typical high-vacuum condition ($<10^{-6}$ Torr) will have less than 1 ppb of oxygen (relative to atmospheric pressure). Therefore the entire optical path, from the shock tube window to the spectrometer, is contained within a high vacuum box, while the spectrometer itself is vacuum rated and also maintained at high vacuum. A nitrogen purge is employed on the camera itself, in the region between the camera window and intensifier. Window materials must be chosen for their wavelength cutoffs : MgF_2 or LiF above 120 nm, sapphire above 150 nm and fused silica above 165 nm. The VUV, UV/Vis and Vis/NIR detectors are all intensified CCD arrays with silicon based photodiodes. Though the shock is bright, the intensifier is necessary to obtain strong signal at low exposure time and with good spatial (i.e. large F/#) and spectral (narrow slit) resolution. Each intensifier has an optimal wavelength detection range, and each of the three detectors use the intensifier corresponding to their intended range. Silicon detectors are not viable further into the infrared, so therefore compound semiconductor arrays (generally referred to as Focal Plane Arrays or FPAs) are used above 900 nm. In the near infrared, InGaAs detectors are used, while the Mid-Wave region uses InSb. There is potentially significant absorption from ambient water vapor and carbon dioxide in the infrared, so an identical optical vacuum box as used for the VUV is employed for these systems. The mid-IR spectrometer is purged with a purge gas generator that removes H_2O. and CO_2 from ambient air. While ordinary glass windows are sufficient for visible through near infrared wavelengths, measurement in the mid infrared requires high wavelength cut off windows - typically sapphire is used in this case.

Calibration of radiance in absolute units is in principle straightforward, but challenging in practice. In principle, it involves imaging a source of known radiance in the same manner as the experiment is to be performed. This is accomplished by having the optical set up on translating rails so that they can be pulled back from the test section. The calibration source is then placed at a position equivalent the tube centerline. Any relative movement of the optical components during the translation may invalidate the calibration, so care must be taken to maintain a stable system during this process. We have generally used three types of calibration sources for this purpose: for visible through near infrared measurement (e.g. 300-2000 nm), an integrating sphere is employed as a uniformly radiating source. We have two spheres of differing diameter (1.5" and 4" port openings), where the 4" sphere is employed primarily and the 1.5" sphere is used at times when the 4" sphere is out for service or re-calibration. The sphere is translated across the length of the window so that the calibration is obtained at different points in the image. The 3-5 images obtained are then stitched together to form a full field calibration. For calibration below 300 nm, a calibrated Deuterium arc source is employed. The Deuterium arc is spatially non-uniform and has a smaller F/# than the spectrometers, so that the optics are underfilled. Thus, the magnitude measured is very sensitive to the positioning of the lamp and the shape of the image will depend upon spectrometer spatial resolution and slit width. For these reasons, it is difficult and potentially erroneous to use the lamp as a standard for absolute radiance calibration. Instead, the lamp calibration is assumed valid in a relative, but not absolute, sense (i.e. the ratio of radiance at two wavelengths is assumed

valid). The calibration measurement is then performed at both the wavelength range of interest and at a wavelength range matched to the integrating sphere (generally 300-360 nm). The calibration is then scaled to absolute units. The lamp is translated at discrete points along the measurement axis to obtain a position-dependent calibration profile. These points are spline interpolated to obtain the final calibration image. In the mid-infrared range, a blackbody cavity is employed. The blackbody is supplied with a NIST certified temperature standard, and the thermocouple reading (which may differ from the standard by tens of degrees) is translated to match the NIST calibration. The blackbody cavity presents a uniform radiance source over a 1" diameter, as described by the Planck equation:

$$B(\lambda, T) = \frac{2hc^2}{\lambda^5 \left(e^{hc/kT\lambda} - 1 \right)}$$

(2.1)

The source is translated, as with the integrating sphere, to obtain a full field calibration. The source, as well as the region between the source and optics box, is purged with the same air source as the MWIR spectrometer to minimize absorption by ambient CO_2/H_2O. Details of these calibrations are given in the following section.

2.1. Calibration Details

The systems require calibration in three quantities, corresponding to the x, y and z axis of the images. The measurements are described below in detail. Another important detail of the x and y calibration is the instrument resolutions, which are discussed in the corresponding sections.

2.1.1. Wavelength calibration

Spectral (x-axis) calibration is performed using atomic line sources such as a Mercury Lamp. The measurement generally involves the measurement of known line locations and fitting the wavelength as a function of pixel row using a second order polynomial. Some example calibrations are shown in Figure 2. In the visible through near-infrared wavelengths, calibration with pen lamps (typically Hg) is straightforward. The spectrometers use built-in routines which determine the calibration over the entire grating range through the measurement of a few lines at the far ends of the spectrum. The result of such a fit is shown in Figure 2(b), where the lines are all matched within 1 pixel (within 2 pixels is typically considered acceptable). Wavelength measurement in the vacuum ultraviolet and mid-infrared poses some additional challenges. Pen lamps are not useable in the VUV due to ambient absorption, instead the Lyman-α peak of a D_2 lamp is used for calibrating the low wavelength end of the spectrum using the spectrometer's built-in routines (Figure 2(a)). Suitable atomic line sources are not generally available in the mid-IR. If the FPA has sensitivity in the near-IR, it is possible to measure 3rd and 4th order diffractions of near-IR lines for wavelength calibration. If the FPA filters lower wavelength signals, as was the case with those employed in our earlier tests, calibration is performed using ambient CO_2 absorption. Measurements made with and without the N_2 purge yield an absorption spectrum which is then fit using a room-temperature simulation of the CO_2 spectrum from the Carbon Dioxide Spectral Databank. The fit requires simultaneous adjustment of bandstrength, instrument broadening factor and wavelength dispersion and offset. The fidelity of this fit only allows for a first-order polynomial calibration of wavelength versus pixel column.
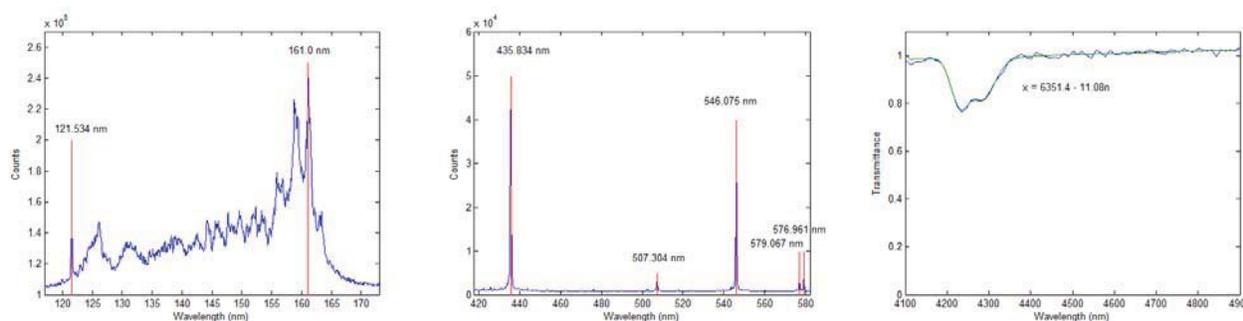
Figure 2. Example wavelength calibration spectra. (a) D2 lamp for VUV calibration, (b) Hg Pen lamp calibration, (c) Linear fit to CO_2 absorption spectrum in IR.

From the spectral calibration data, it is also possible to obtain the instrument resolution function, also referred to as *Instrument Lineshape* (ILS). This is a critical parameter for obtaining comparisons to spectral data and incomplete or approximate characterization of this function may lead to misleading results. The measurement of the ILS assumes the broadening of the pin lamp itself may be considered infinitesimally thin, so that an individually measured line will describe this instrument function. Typically, the fit must be performed on a calibration image using the sum of multiple instrument lines, plus a baseline function. For the best possible fit, it is important to include both weak and overlapping lines. If a (sufficiently bright) spectral line source is not available in or near the wavelength of interest, the measurement of the spectrometer zero-order line may substitute for this characterization -- this is typically the case in the mid-infrared. In general, the ILS must be re-measured any time the spectrometer is altered in terms of its focus, slit width, grating resolution or grating location. For a set of experiments where all these items are held constant, the same instrument function will likely hold.

The instrumental resolution function is found to be empirically described by one of three functional forms. Traditional triangular functions have been found to be insufficient. With the intensified CCD arrays, neither Gaussian nor Lorentzian functions adequately capture the instrument function, which is found to decrease in intensity as $\Delta\lambda^{-1}$, where $\Delta\lambda$ is the distance from the line center. This gradual roll-off has led to the empirical formulation of the square root of a Voigt function to describe the lineshape, which will display this dependence far from the line center:

$$G\left(\Delta\lambda;\lambda_G\right) = \sqrt{\frac{\ln 2}{\lambda_G^{\;2}\pi}}\exp\left(-\ln 2\left(\frac{\Delta\lambda}{\lambda_G}\right)^2\right)$$

$$L\left(\Delta\lambda;\lambda_L\right) = \frac{1}{\pi}\frac{\lambda_L}{\Delta\lambda^2 + \lambda_L^{\;2}} \qquad (2.2)$$

$$V\left(\Delta\lambda;\lambda_G,\lambda_L\right) = \int_{-\infty}^{\infty} L\left(\Delta\lambda;\lambda_L\right)G\left(\Delta\lambda - w;\lambda_G\right)dw$$

$$ILS_1\left(\Delta\lambda;\lambda_G,\lambda_L\right) = \left[V\left(\Delta\lambda;\lambda_G,\lambda_L\right)\right]^{\frac{1}{2}}$$

This dependence has been found particularly suitable for the VUV and UV/Vis cameras. The VIS/IR camera is generally fit by this function, but shows a somewhat better relationship using a linearly weighted average of Gauss and Lorentzian functions:

$$ILS_2\left(\Delta\lambda;\lambda_L,\lambda_G,r\right)=\frac{G\left(\Delta\lambda;\lambda_G\right)+10^r L\left(\Delta\lambda;\lambda_L\right)}{1+10^r} \tag{2.3}$$

The infrared focal plane arrays tend to be well characterized by a Gaussian dependence in most cases. The Gaussian is a special case of $ILS_2\left(\Delta\lambda;-,\lambda_G,-\infty\right)$. In some cases, however, when large slit widths are required to capture sufficient intensity, the lineshape displays a flattened top and is not well described by any of these functions. In this case, the opening of the slit acts as a square function, while the edges display the Gaussian shape expected for a narrow slit. Therefore, the ILS is well-described by a convolution of a Gaussian with a square function. This ILS, described as a *Smeared Gaussian*, is given by the following formula, using the well known error function, *erf*:

$$erf\left(x\right)=\frac{2}{\sqrt{\pi}}\int_0^x e^{-t^2}\,dt$$

$$ILS_3\left(\Delta\lambda;\lambda_G,a\right)=\int_{-a}^a G\left(\Delta\lambda+w;\lambda_G\right)dw = erf\left(\frac{\Delta\lambda+a}{\lambda_G}\right)-erf\left(\frac{\Delta\lambda-a}{\lambda_G}\right) \tag{2.4}$$

Correct measurement of any ILS function requires the slit be uniformly illuminated (i.e. overfilled) during measurement. This may be become problematic for large slit settings. Whether or not the slit is overfilled can be seen by translation of the source from left to right (perpendicular to slit) -- if the slit is underfilled, the linehsape and peak position will change as the source is moved. An underfilled slit may be remedied by changing the distance between the spectrometer and calibration source, or by using a larger area source.

It should be noted that these three functions, as given here, are not normalized to any particular value. Application of these functions to a predictive simulation would require numerical normalization so as to conserve energy. For the purposes of providing an instrument function, however, providing the functional shape within a constant scaling factor is sufficient. Examples of these three fits are given in Figure 3.
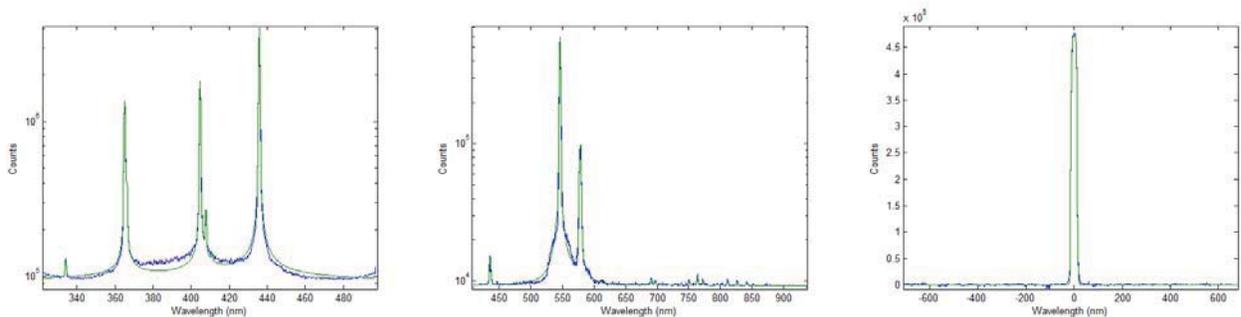
Figure 3. Sample lineshape fits, (a) Hg calibration lamp image fit with square root of Voigt function, (b) Averaged Gaussian and Lorentzian function for Hg/Ar lamp, (c) Smeared Gaussian fit of zero order signal on mid-wave infrared FPA.

2.1.2.   Spatial Calibration

Spatial (y-axis) calibration is performed by imaging a ruled image - this is done by either illuminating an opaque ruled paper, placed at the focal plane, or by placing a ruled transparent marker in front of an illumination source at the focal plane. In either case, an image with distinct horizontal lines from the ruled object is obtained, and a

linear relation of cm/pixel is derived. Samples of both of these are given in Figure 4.
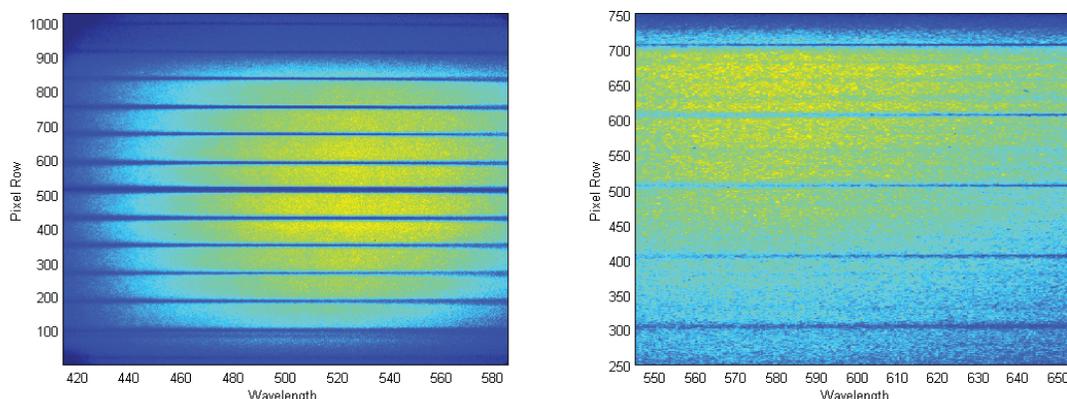
Figure 4. Sample Position calibration images. (left) Image of a back-illuminated acrylic window with 1 cm rulings, (right) Front-illuminated paper with 1" ruled marking

The *spatial resolution function* (SRF) describes the resolution of the image in the y-direction. In our case, the SRF is composed of three principal components: the resolution of the optics, the resolution of the CCD array and motion of the shock wave during camera acquisition.

The optical resolution is estimated by using geometrical optics. This can be performed by a ray-tracing analysis of the optics through the maximum aperture of the system. In our case, the optics are specified to be larger than the F/# of the spectrometer, so the aperture is determined by the spectrometer F/#. Ray tracing for the three optical designs is shown in Figure 5. In this image, the angles of the mirrors have been unfolded, so that the ray is traced on a single axis. This causes flat mirrors to be absent from the plot, while the powered mirrors will change the directions of the rays. The figure starts from the spectrometer at x = 0. From there, the points corresponding to the top, middle and bottom of the CCD array, as re-imaged on the spectrometer slit, are shown. From here, the collection volume expands outward according to the spectrometer F/#. At the first mirror, the image is re-focused as per the lensmaker equation. For the VUV, UV/Vis and Vis/IR spectrometers, this mirror is placed very close to its focal point, so that the image focuses near infinity, and thus the rays continue parallel to one another (Figure 5(a)). The angle of the rays is then determined by the height of the object. The second powered mirror focuses these rays again back into the shock-tube. Since the incoming rays are collimated, they will converge to the focal point of the mirror, which is positioned to the center-line of the tube. This is described as a *telecentric* configuration. The light collected from the shock tube will then be described by the area between the two rays inside the tube. For all positions, these rays form triangles whose axes are perpendicular to the tube. The optical resolution function is therefore approximated as a triangle of the same width as these rays. This is shown in Figure 5(b). Appendix A presents a more detailed derivation of the optical shape.
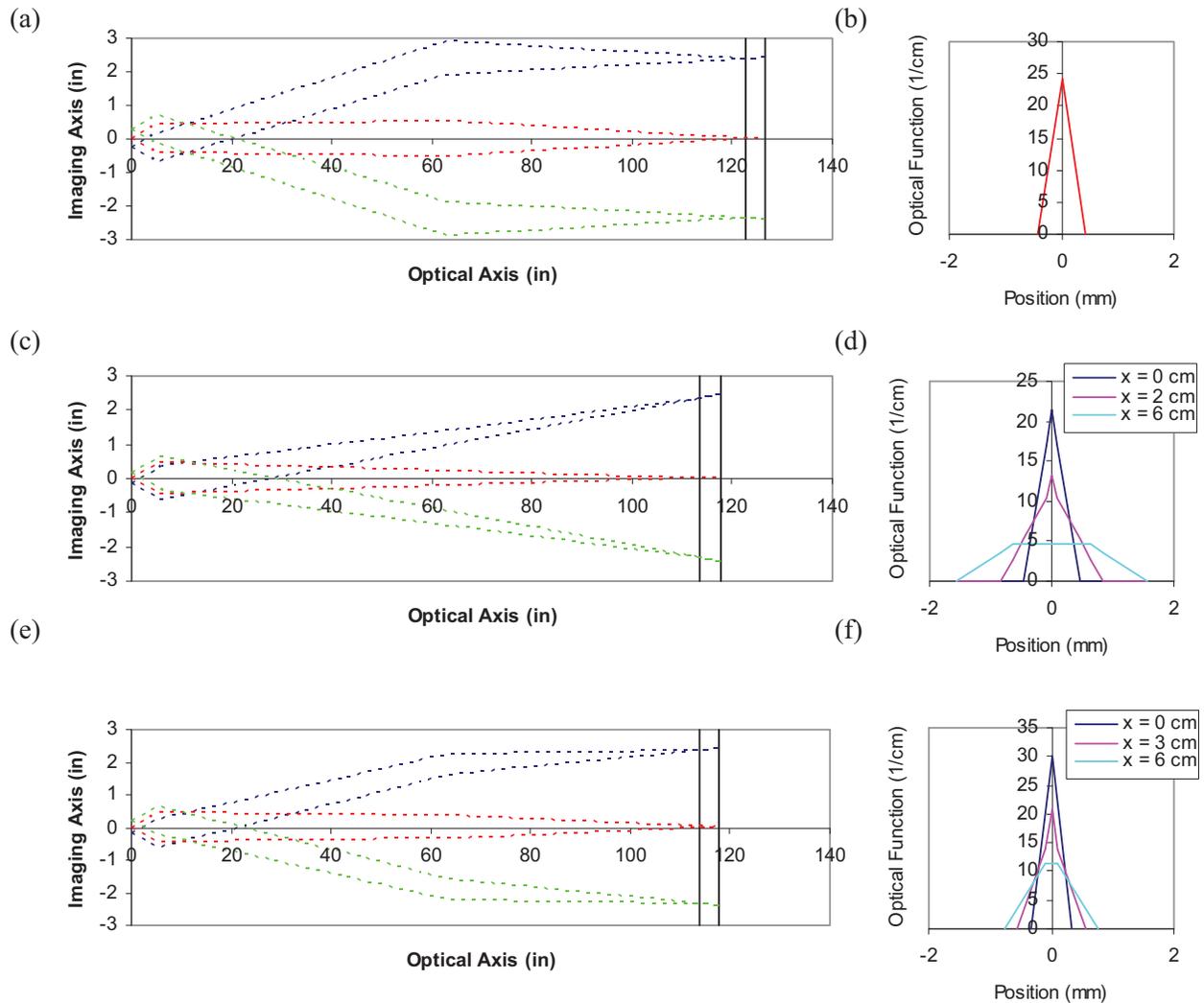
Figure 5. (a,c,e) Unfolded optical paths. x-axis follows the length along the optical path, y-axis shows the extent of the optical collection volume normal to the path. The three different color traces indicate how this volume extends from the centerline and far edges of the CCD. The tube wall is shown by the vertical solid lines. (a) VUV, UV/Vis and Vis/NIR, (c) NIR, (e) MWIR. (b,d,e) shows the corresponding (approximated) optical resolution function.

For the NIR optic, a higher magnification (approximately 2x) is required. A telecentric configuration for this magnification is impractical as it would require twice the path length. A telescopic configuration was utilized instead. In this case, only a single mirror is applied, and the lens-maker equation $(1/a + 1/b = 1/f)$ is used to place the images at both the shock tube center and at the spectrometer slit. Tracing the rays through these two points, with angles determined by the spectrometer F/#, gives the trace in Figure 5(c). In this case, the center-line image forms a triangle whose central axis is perpendicular to the tube, but on the outer edges, this axis is skewed. The optical line shapes are then position dependent, as shown in Figure 5(d) and described in greater detail in Appendix A. For evaluation purposes, we use the worst case (off-center) line shape, which is approximated by a trapezoid. The MWIR optic, having a magnification slightly greater than the UV/Vis

systems, utilizes a configuration which is nearly, but not quite, telecentric (Figure 5(e)). Here, the imaging angle is tilted relative to the tube axis, but not severely. The corresponding approximate resolution functions are shown in Figure 5(f), and in the worst case is trapezoidal.

The second effect has to do with the spatial resolution limits of the CCD camera. This effect is similar to the instrument line shape function, in that it may be determined by the combination of non-ideality in the optics and spectrometer with the charge sharing between adjacent pixels on the CCD array. Therefore, the camera portion of the spatial resolution function is generally fit well by the same functional forms applied for the instrument lineshape. This function is experimentally determinable by imaging the edge of a calibration source. The edge must be well defined so as to create a sharp transition, the deviation from which may be characterized as an instrument function. For the calibration source placed at the sagittal focus, the transition may be assumed reasonably sharp. (For an astigmatic optical design, the sagittal focus would be the tube centerline). Otherwise, a straight edge may be placed in front of the calibration source to simulate the sharp transition. An example of this is shown in Figure 6. The deviation is visually apparent, and is most easily analyzed by taking the derivative of the signal. The derivative is then fit with the ILS_1 functional lineshape. This fit, being experimentally measured, will take into account all of the non-idealities of the optical and camera system. As long as the calibration source is at the tangential focus (i.e. equivalent spacing as the tube centerline), the optical resolution function will not be included in the measurement, since that function describes the radiance collected over the entire diameter of the tube (i.e. off-centerline).
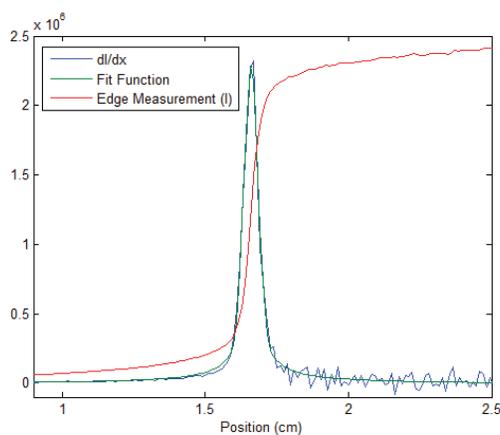
Figure 6. Determination of the camera contribution to the spectral resolution function. The derivative of the edge of the calibration source measurement is differentiated to obtain the resolution function.

The final affect in the spatial resolution has to do with the fact that the shock is in motion while the camera is shuttering. This results in a loss of resolution which to first order may be approximated as the product of the shock velocity and the gating time. As an order of magnitude estimate, a 10 km/s shock will move 1 cm in a μs. Therefore, gating times are typically held to less than 1 μs, but the signal levels on the camera often prevent us from going much below this level. In terms of the spatial resolution function, this approximation would correspond to a square wave of this length. This, however, assumes that the camera gates as a square pulse. For long exposure times, this is usually a safe assumption, but in the sub-μs regime it is not. The gating function can be measured experimentally using a pulsed light source at varying delays to the camera trigger. For accurate

measurement, the source would need to gate faster than the desired resolution of the gating function. We have used both pulsed LED and laser sources to measure the gating for several of the cameras. The measurement on some of the ICCDs is shown in Figure 7. In Figure 7(a), it can be seen that the camera gain experiences a ringing at the beginning of the exposure, which decays as the gain approaches its steady state level. In Figure 7(b), the resolution is too low to observe the ringing, but the overall shape of the function is seen to be significantly different from a square. The spatial resolution function then is given by the product of this function with the shock velocity. We have found this signal may be fit by an equation of the following form:

$$f_{mot}(\Delta y) = \begin{cases} 1 + A\sin\left(\omega\dfrac{\Delta y}{v}\right)\exp\left(-\dfrac{\Delta y}{v\tau_1}\right) - B\exp\left(-\dfrac{\Delta y}{v\tau_2}\right) & 0 < \dfrac{\Delta y}{v} < t_{gate} \\ 0 & otherwise \end{cases} \quad (2.5)$$

which is a 5 parameter fit. At present, this function has only been measured on three of our cameras, and will be further characterized in the future. In the interim, square gating functions may be applied.
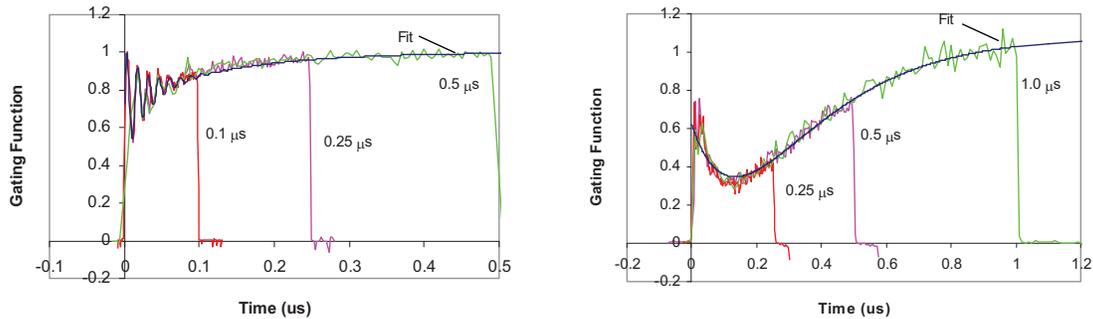
Figure 7. Experimentally measured gating function for the (a) VUV and (b) Vis/NIR cameras. The function in (b) was measured at ~10x lower resolution than (a).

With knowledge of these three functions, the overall spatial resolution function can be found by convolving all three functions:

$$SRF(x) = f_{opt}(x) \otimes f_{cam}(x) \otimes f_{motion}(x) \quad (2.6)$$

An example of this convolution is given in Figure 8. The function typically appears to be dominated by the camera function, though the motion will provide a noticeable broadening beyond this. The optical function has much less significant impact on the resolution. It is our practice to provide spatial convolution functions for every shot collected in EAST, and these are now archived with the data sets.
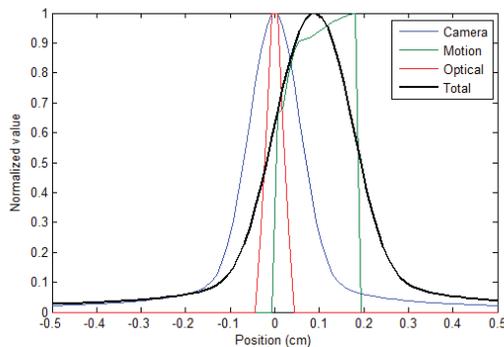
Figure 8. Sample spatial resolution function

2.1.3. Radiance Calibration

While the calibration is in principle simple, there are several details to be considered. At the simplest level, a number of counts is obtained for a known radiance, and thus a calibration factor with units of radiance per count may be obtained. When the actual measurement is then taken, the number of counts measured is multiplied by this factor to obtain a measurement in absolute radiance. However, several assumptions and artifacts must be accounted for and will be described in detail through an example.
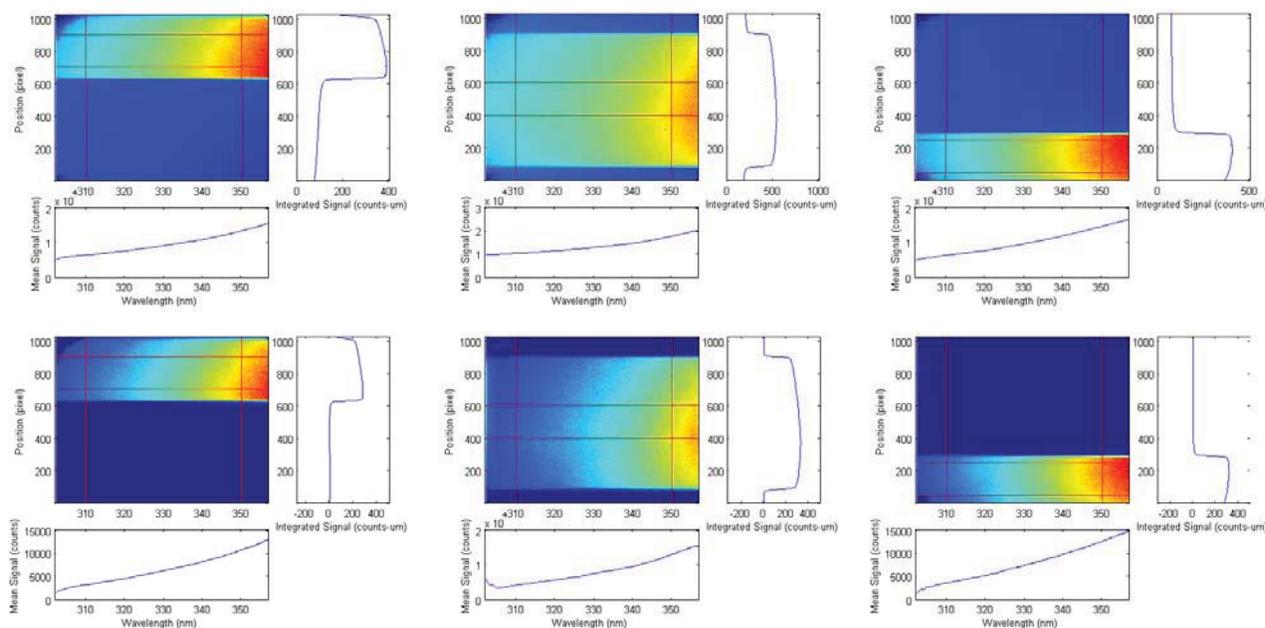
Figure 9. Images of raw calibration data (top row) and after pedestal correction (bottom row)

A typical measurement with the integrating sphere in three locations is shown in Figure 9. The x calibration is included in the data file as obtained from the instrument software, while the y calibration is applied at the end of the process. The intensity of the image is in units of counts. The vertical cross section shows the integral of this

image over the range marked with red vertical lines, while the horizontal cross-section shows the mean value between the horizontal lines. The location of the integrating sphere source is visible by the location of the step change in signal, however it is apparent that signal is also present on either side of the integrating sphere source. This signal is due primarily to scattered light within the spectrometer and is referred to as *pedestal*. The pedestal is typically strong on the VUV and IR spectrometers, but weak on the visible ones. The pedestal usually shows some wavelength dependence, so must be corrected column by column. Pedestal corrected images are shown in the second row of Figure 9. The pedestal correction is visually imperfect near the edge of the CCD, where the dark corner regions make linear fits to the pedestal difficult. The calibration routine does attempt to remove the dark sections, though unambiguous definition of these regions is not always straightforward.

Following pedestal correction, the counts are divided by the calibration function of the instrument. Here, there are several options. All calibration sources are traceable to standards provided by calibration labs. However, the sources are also equipped with monitors to check and compensate for source drift. The large integrating sphere used here has both broadband and spectral monitors. For this particular calibration, the spectral monitor result is shown plotted next to the manufacturer calibration in Figure 10. Some drift is evident, particularly at low wavelength, though it is not possible to confirm whether the drift is in the calibration source or in the monitor. For now, the spectral monitor is assumed more accurate and the spectra are scaled by this function to obtain a response function in units of counts/radiance. The images calibrated by this function are shown in Figure 10.
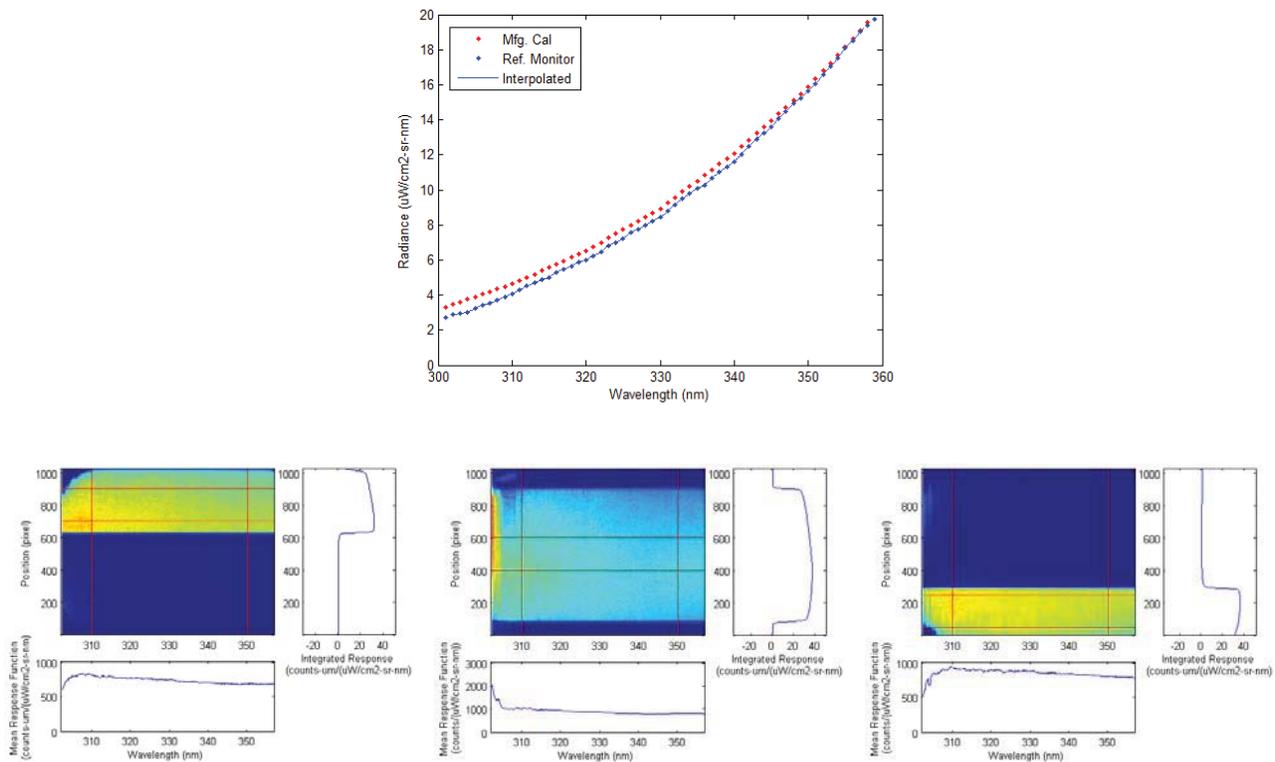
Figure 10. (top) Calibration curve as supplied by the manufacturer and measured by the spectral reference monitor. The solid line is a linear interpolation of the reference monitor to the x-spacing of the spectrometer calibration. (bottom) Spectral response functions obtained from the calibration curve

This calibration is now valid at the exposure time used for the calibration, however, the test, being much brighter than the calibration source, is to be performed at a lower exposure time. It is then necessary to apply an exposure time correction. A simple approximation would be to multiply by the spectral response by the ratio of exposure times, however this approach is not always correct as the intensity may not vary linearly with exposure time. The deviation of intensity on exposure time from linearity is here referred to as *non-reciprocity*, and is corrected by the use of a *reciprocity factor*. The reciprocity factor can be determined by a few different means. The most straightforward is to measure the intensity of the light source at different exposure times and obtain the ratio directly. This may be done with the spectrometer slit at a wide setting so as to obtain sufficient brightness. In this way, a reciprocity curve is obtained that may be used to correct the data. (see Figure 11(b)) A second method is to measure the gating function of the camera. This measurement was discussed in Section 2.1.2 and shown in Figure 7. (Note the gating function has been normalized to approach 1 at long times.) The integral of this gating function would equal the measured intensity. Dividing the exposure time by this integral yields the reciprocity factor displayed in Figure 11. The response functions in Figure 10 are then multiplied by ratio $\tau_{exp} r(\tau_{cal})/\tau_{cal} r(\tau_{exp})$, where τ is the exposure time for the experiment and calibration and $r(\tau)$ is the reciprocity factor at this time. This yields the response function at the experimental condition.
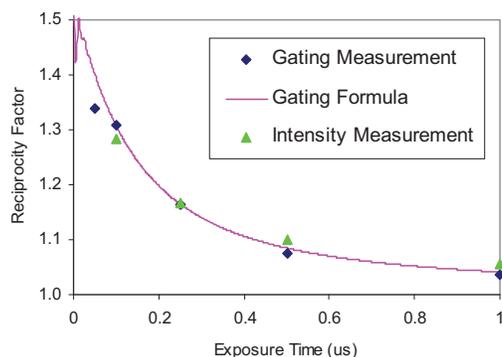
Figure 11. The reciprocity factor as determined by the integral of the gating function and ratioing of intensity measurements.

Next, these three (or more images) are combined together to yield the composite response function. Only the bright part of each image is retained - in regions where bright regions overlap they will be averaged together. Should the regions fail to overlap due to misplacement of the light source during calibration, the region between may be interpolated. Care must be taken to exclude regions near the end of the image, where the intensity "rolls off" due to finite spatial resolution (e.g. Figure 6). The stitched image is shown below in Figure 12. The composite image may show stitching artifacts in regions where this roll off is not accounted for or a bad pedestal correction is obtained. This kind of artifact is clearly apparent at the low wavelength range of the image. When this occurs, additional corrections to the calibration may be necessary. An additional factor applied to Figure 12 is the removal of dark points in the response function. This is done by setting all points below the image's noise threshold to infinity and is apparent in the brown corner regions of the response function. This is done so that, when the final calibration is performed by dividing in the response function, these points will be zero rather than taking on some large non-zero values.
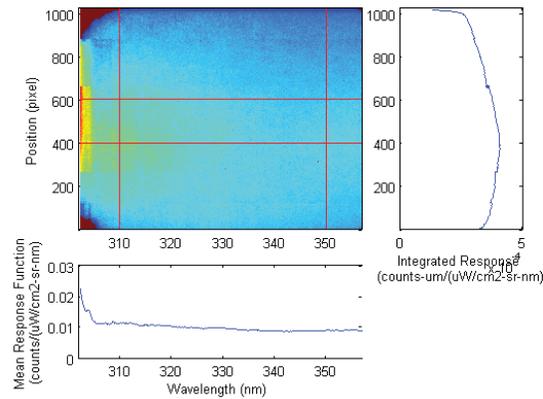
Figure 12. Final Calibration Function

For wavelengths above 300 nm, the process so far would represent a complete calibration of the camera. However, for lower wavelengths, this process serves as a reference calibration. Since the deuterium lamp required to calibrate at these wavelengths underfills the camera optics, the reference calibration described above is used to scale the deuterium calibration. The Deuterium lamp calibration is performed at both the desired calibration range and at the reference range, as shown in Figure 13. As can be seen, this calibration yields a highly peaked image in the y-dimension. This calibration is performed at typically 20 equispaced positions on the y-axis. The D_2 lamp image shows some small pedestal: this is corrected column-by-column and is relatively straightforward due to the pedestal being much weaker than the peak intensity. The difference between the raw and pedestal corrected data is seen through the red and blue lines in the cross-section data.
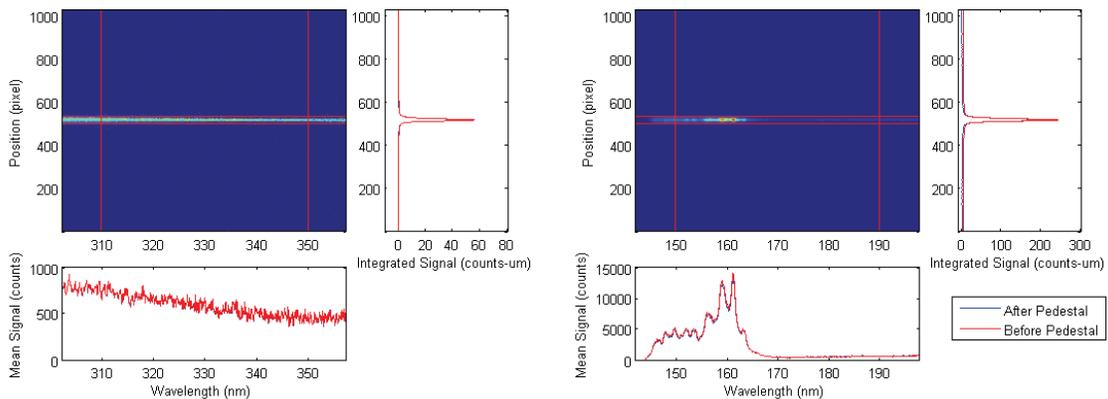
Figure 13. Sample Deuterium Lamp calibration images (left) reference wavelength (right) calibration wavelength

In the reference wavelength range, the response function obtained with the integrating sphere is applied, Figure 14(a). This gives a signal in units of radiance, however since the optics are underfilled it is not the true radiance of the source. In order to avoid artifacts from the instrument resolution, this calibrated image is summed over the y-dimension, resulting in a spectral radiance weighted by some spatial factor. This is performed for each of the 20 images obtained to give the low resolution image in Figure 14(b). Each row in Figure 14(b) represents

the result of one calibration image.
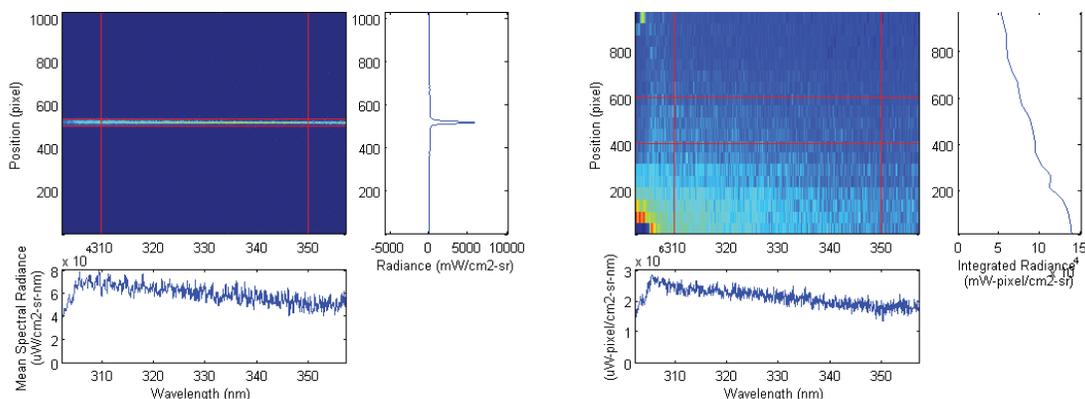
Figure 14. (left) A single reference image with calibration function applied. (right) The composite of 20 reference spectra calibrated and integrated over y to give a low-resolution spatially weighted radiance.

The spatial factor can then be extracted from each row by scaling the spatially weighted radiance to match the calibration spectrum of the lamp. This process is demonstrated in Figure 15 for one row of the low resolution image. A least squares minimization of the spatial factor gives the best overlap of the calibrated data with the reference spectrum. (Figure 15(a)) An obvious inconsistency in this scaling is apparent due to the quality of the reference calibration at low wavelength. To prevent this from biasing the fit, the low wavelength ends of the data are successively removed until the calibration curve is contained within the noise of the data. (Figure 15(b)) In this way, a scaling factor is obtained for each y-point measured. (Figure 15(c))
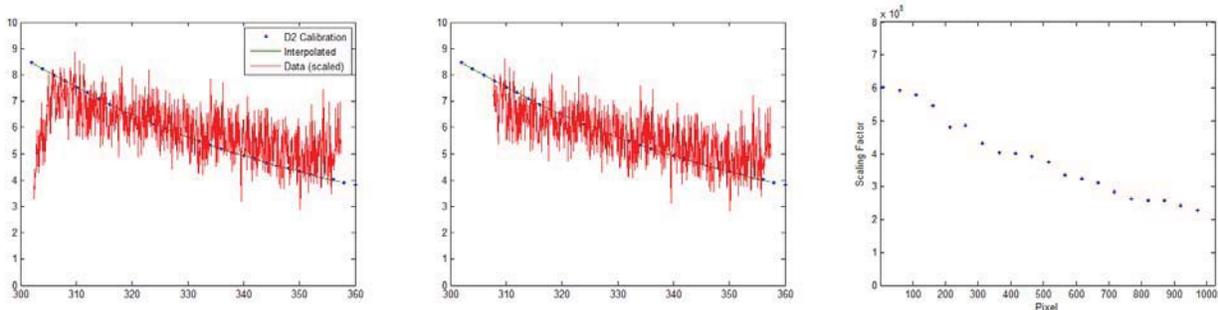
Figure 15. Extraction of the spatial factor. (a) Initial scaling of radiance to match the calibrated radiance curve. (b) Refined scaling by neglecting outlying edge points. (c) Scaling factor obtained as a function of y-pixel position

Similarly to the reference spectrum, the calibration spectrum is also pedestal corrected and summed as shown in Figure 16(b), to give a measurement in counts, weighted by a spatial factor. In order to obtain the response function it is next necessary to divide by the spectral function of the calibration source and the spatial factor. The calibration source is strongly peaked by wavelength, such that small misalignments in x may create vertical bands in the calibration. These are pre-emptively removed by shifting the spectrum slightly so peaks are aligned. (Figure 16(a)) The spatially weighted counts are then divided by the lamp calibration function to obtain

a spatially weighted response function, Figure 16(c). Finally, the spatial factor, having been obtained from the reference image, is then removed to yield a low resolution (20 x 1024) response function (Figure 16(d)).
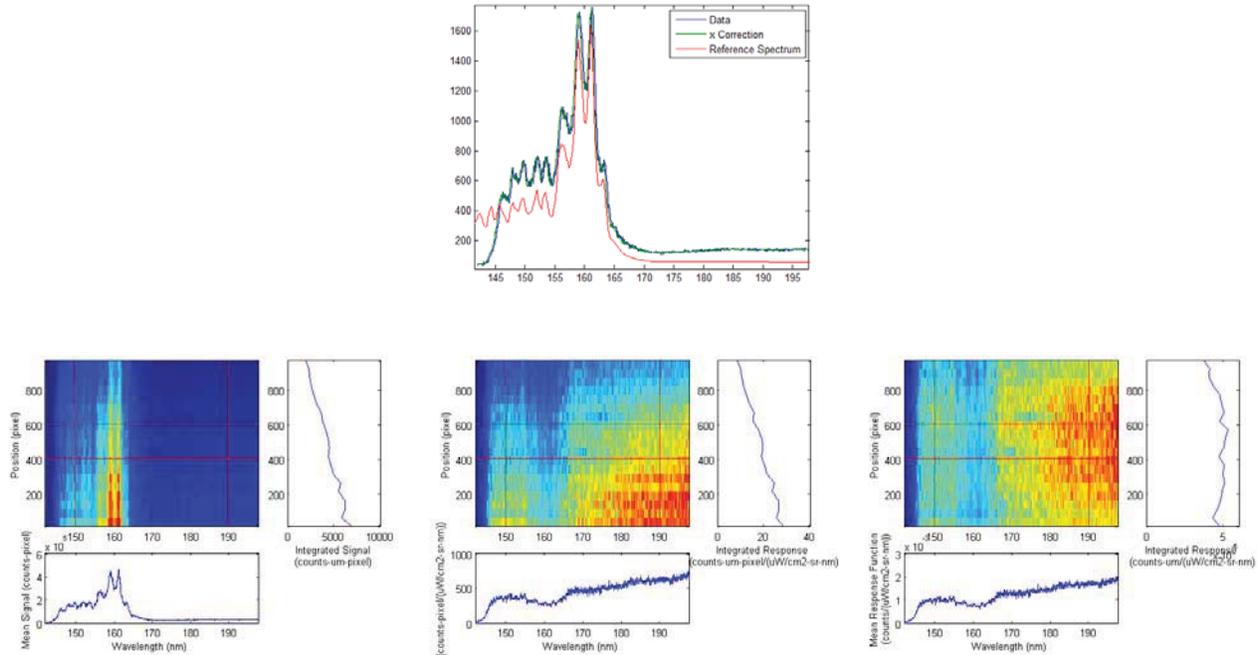
Figure 16. (a) Demonstration of the x-shifting of calibration data to align with the reference spectrum, (b) Composite image of summed calibration signal, (c) Response function with spatial factor, (d) Low resolution response function.

In the final step, the low resolution response function must be interpolated to the high resolution (1024 x 1024) of the camera. Rather than using a direct interpolation of the low resolution function, it is desirable to make use of the spatial dependence known from the full field calibration. To do this, the function is assumed to be of the form $RF(x,y) = RF_x(x)RF_y(y) + RF_{xy}(x,y)$, without loss of generality. For discussion, we will refer to the separable portion RF_xRF_y as a *flattening function*, and the remainder, RF_{xy}, as the *flattened response function*. The flattening function is shown in Figure 17(a), and its constituent x and y functions can be seen in the cross sections of Figure 17(a). The separable y component, shown in the vertical cross section, is assumed to be proportional to the sum of the reference spectrum over its columns. The x component (which also contains the proportionality factor) is determined by applying a least squares minimization of the RF_xRF_y product to the low resolution response function. This result can be seen as the horizontal cross section of Figure 17(a). This flattening function is next removed from the low resolution function, yielding a low resolution flattened response shown in Figure 17(b). The flattened response is then interpolated to high resolution with a piecewise cubic spline, then added to the flattening function to obtain the high resolution response function. (Figure 17(c))
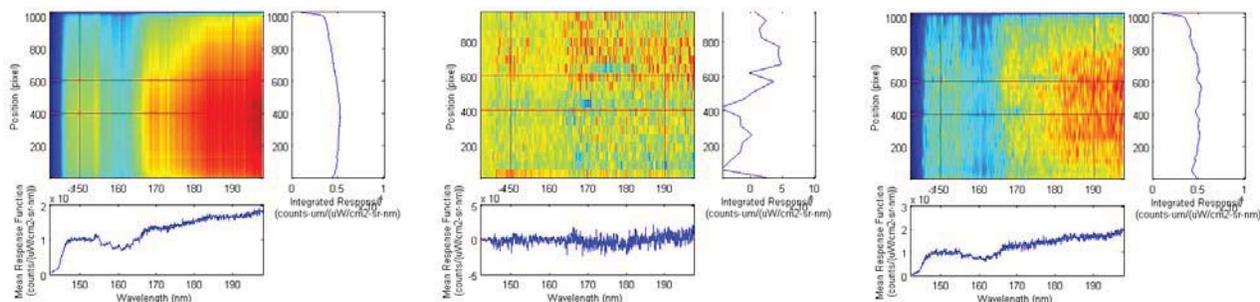
Figure 17. Interpolation from Low Resolution to High Resolution. (a) Flattening function obtained by multiplying y- and x- dependent functions. (b) Flattened response function obtained by subtracting the flattening function from the low resolution response function. (c) Final response function obtained by adding a spline interpolation of the flattened response to the flattening function.

The final calibration image in Figure 17 clearly has some low frequency noise as a result of the interpolation. Smoothing steps have been considered to improve the noise, though this step is typically omitted as it does not substantially improve the calibration quality. There is also a clearly a dip in the response function near 160 nm where the lamp signal is at its maximum. This may be due to some drift in the lamp's calibration or non-linearity in the camera response. At present, this dip is retained in the calibration, as there would be no demonstrable accuracy to removing this feature. (i.e. it is not known whether the "true" calibration lies at the top or bottom of this feature.) To remove this uncertainty, a smoothly varying source would be highly preferable to the peaked output of the D_2 lamp, though such sources are not readily available at this time.
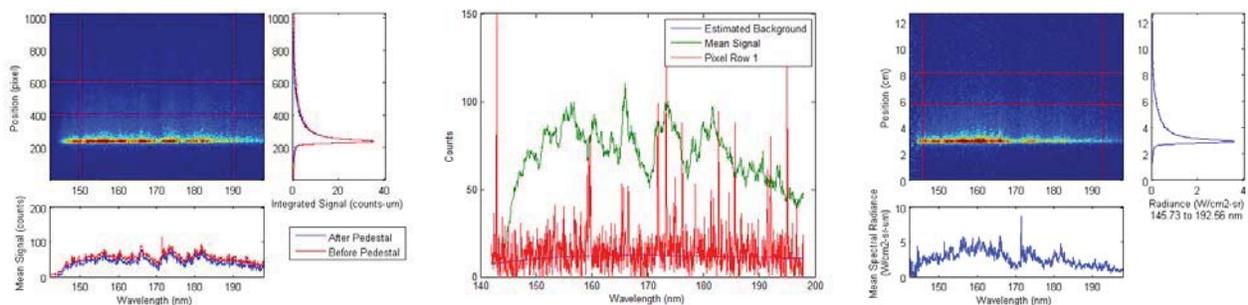
Figure 18. (a) Raw data before and after scattering correction. (b) Illustration of scattering correction relative to other camera signals. (c) Final calibrated data.

With the existence of a calibration function, the collected data can now be converted to absolute units. Figure 18(a) shows the raw data obtained during the test. Just as the calibration images suffer scattered light that must be removed via pedestal correction, a similar correction must be performed on the shot data for the VUV and IR cameras. (This is optionally performed with the visible cameras which have small levels of scattering). In order to do this, it is assumed that a nominally dark region exists on the camera, typically in front of the shock wave. The pixel rows are binned in groups of 5 and the one with the smallest magnitude is fit with a third order polynomial. This polynomial fitting is necessary to prevent the noise in the 1-d spectrum from appearing as vertical streaks in the image. Figure 18(b) shows this polynomial fit in comparison to the mean signal on the camera and the signal on the first pixel row. The data after removal of this scattering function is shown in Figure

18(a) - the impact can be seen by comparing the plotted cross-sections. This corrected data is then divided by the response function and the linear y-axis calibration is applied to obtain the final data. (Figure 18(c)).

3.0 RESULTS

Since the upgrade of the EAST facility in 2008, eight test series have been conducted, each containing between 21 and 124 shots. This includes three tests in Air/Earth entries, four tests for Martian ($CO_2/N_2/Ar$) entry and one test for Venus (CO_2/N_2) entry. The nature and objectives of the tests are summarized in Table I. Also shown in the table is the number of shots performed for each test. In any given test series, some fraction of tests will be unusable due to insufficient test time, triggering errors, etc. This is accounted for in Table I by showing both the number of shots performed and the number of shots which had at least one useable spectrometer image. In each test series (except 53), four spectrometer/cameras were in use for most shots, so the total number of data sets from the below tests is in excess of 1,300.

Table I. EAST Tests since 2008

Test	Duration	Planetary Environment	Gas Mixtures (Molar Ratios)	Conditions Spanned	Purpose	Number of Good Shots/ Total Shots
Test 47	Dec 08-Jul 09	Earth	N_2/O_2 (79/21)	8.9-10.1 km/s 0.1- 0.7 Torr	Facility Baselining	40/63
Test 48	Jul 09-Jun 10	Mars	CO_2/N_2 (96/4)	1.3-9.7 km/s 0.01-1.0 Torr	Martian Entry	58/73
Test 49	Aug 09-Oct 09	Venus	CO_2/N_2 (96.5/3.5)	6.4-12.2 km/s 0.5-2.0 Torr	Venus Ballistic	21/27
Test 50	Dec 09-Sep 10	Earth	N_2/O_2 (79/21)	8.0-12.0 km/s 0.1-1.0 Torr	Lunar Return	113/124
Test 51	Feb 11-May 11	Mars	CO_2/N_2 (96/4)	5.7-8.0 km/s 0.05-1.0 Torr	Low Density Mars	36/52
Test 52	May 11-Jun 11	Earth	N_2/O_2 (79/21)	11.3-15.5 km/s 0.1, 0.2 Torr	High Velocity Development	14/21
Test 53	Jan 12-Aug 12	Mars	CO_2/N_2 (96/4)	6.4-8.6 km/s 0.01-0.1 Torr	24" Tube Checkout	29/45
Test 54	Aug 12-Apr 13	Mars	$CO_2/N_2/Ar$ (95.8/2.7/1.5) CO_2/N_2 (96/4) CO_2 (100)	3.0-8.1 km/s 0.05-1.0 Torr	Chemistry Variations	77/89

Figure 19 shows graphically the tests performed, as test points in terms of pressure (in the laboratory) and shock velocity. For comparison, trajectories of flown and planned missions to Mars and Venus and re-entering Earth are overlaid as solid and dashed lines. In these cases, the pressure at altitude has been scaled to match the density in the laboratory test environment.
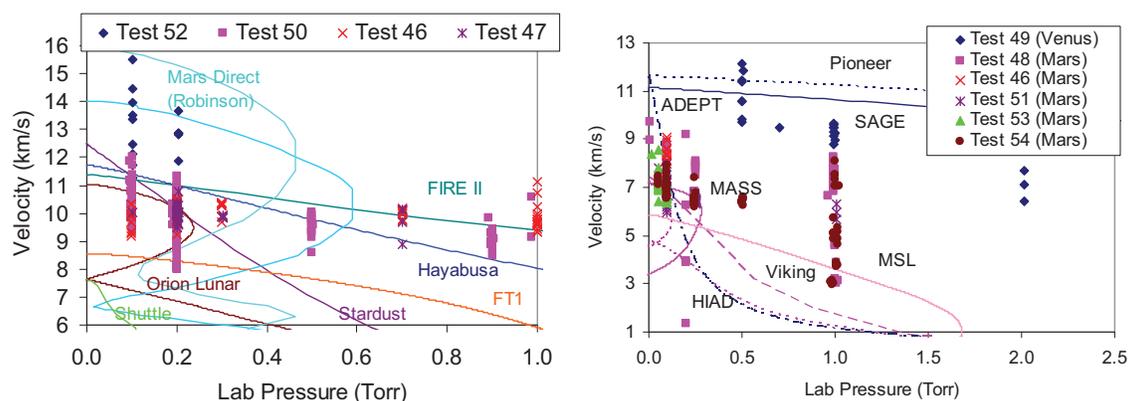
Figure 19. Figures showing the range of EAST Tests conducted since 2006 in terms of velocity and freestream pressure. For comparison, several candidate trajectories are shown (at density equivalent pressure). (a) Air entries, (b) Venus/Mars (CO_2/N_2) entries

As discussed in Section 2.0, the data obtained in EAST takes the form of spatially and spectrally calibrated radiance data. An example of such data is shown in Figure 20, where the spectral resolution is shown on the x-axis and the spatial resolution is given on the y-axis. Typically the data is analyzed in the form of cross-sections taken in one of the two directions. A cross-section in the x-direction gives the spectral features at some distance behind the shock. Often, this is useful for analyzing equilibrium data, in which case an average over adjacent rows may be used to increase signal to noise ratio. This is the type of data shown in the horizontal cross-section plot, and has units of spectral radiance (W/cm^2-sr-μm). Data in the y-direction may be used for kinetic analysis or studies of non-equilibrium radiation in the shock wave. In this case it is convenient to integrate over the y-direction for a single spectral band, feature or group of features. This yields the data shown in the vertical cross-section, and has the units of radiance (W/cm^2-sr) over a given spectral range. These types of analysis will be discussed in turn in the following section.
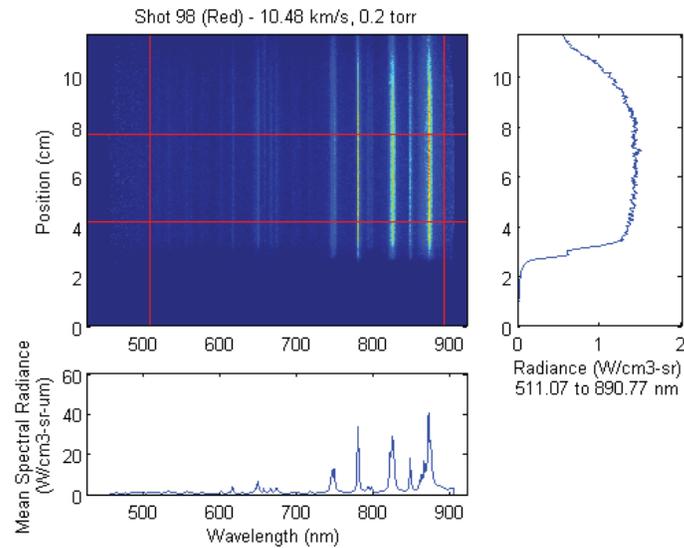
Figure 20. Example of 3D EAST Data (center plot), having spectral radiance as a function of position and wavelength. Horizontal cross-section shows the mean spectral radiance between the red horizontal lines and vertical cross-section has the radiance between the red vertical lines.

3.1. Spectral Analysis

For "equilibrium" analysis, a region behind the shock which is nominally in steady state is selected and averaged. It is possible, using the four different spectrometers over two shots which are at nominally the same condition, to produce a composite spectrum of equilibrium radiance. Such an analysis is shown in Figure 21, which includes composite spectra obtained for Lunar Return Air (10 km/s and 0.2 Torr), a proposed Aerodynamic Decelerator trajectory into Mars (6.5 km/s, 0.25 Torr) and Ballistic Entry to Venus (9.5 km/s, 1 Torr). Distinct features are apparent in each entry condition. The air condition nearly fully dissociates all of the molecules, leading to a spectrum dominated by atomic N and O, with prominent features in the near infrared (700-1200 nm) and vacuum ultraviolet (120-170 nm). The magnitude of the VUV peaks are so high compared to the infrared so as to require a logarithmic scale on the plot. However, the multitude of NIR peaks are large enough as to make their contribution to the overall radiance (shown as a dashed line on the plot) of somewhat larger significance. Underlying the rest of the spectrum is a background continuum which originates from ion-electron recombination (i.e. bound-free radiation.) In the Venus entry experiments, the energy of the shock is again sufficiently large so as to dissociate most molecules. The resulting spectrum has a significant background continuum, accompanied with several atomic lines attributable to C, O and N along with some radiation from the CN radical. The larger density encountered in Venus entry causes the radiation to be generally larger than for air entries. The Martian entry conditions, however, are less severe than either of these cases. While the CO_2 may be fully dissociated, significant fractions of CO and CN are present in the flow, which contribute radiation in the VUV and UV parts of the spectrum. The overall magnitude of radiance for Mars entry make it less relevant in terms of total forebody heat flux as compared to higher velocity entries. However, in cases where the shock standoff distance is large (i.e. large vehicles), this magnitude may become significant.
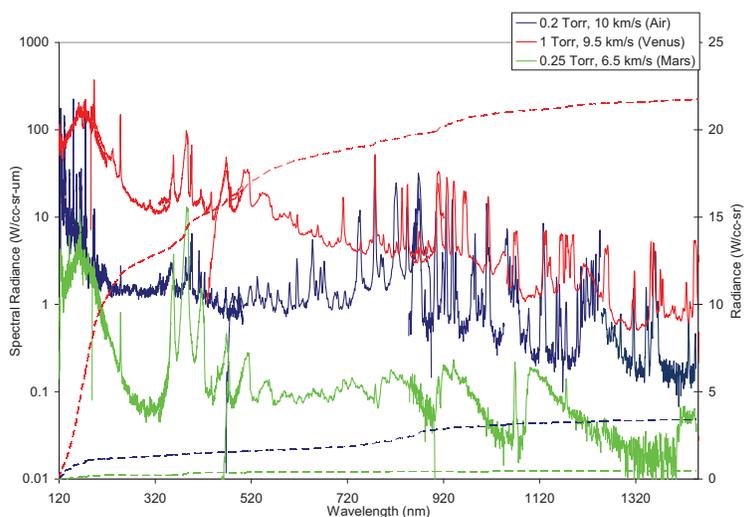
Figure 21. Composite "equilibrium" spectra obtained from Air, Venus and Mars entries. Solid lines depict the spectral radiance while dashed lines show the radiance (integral of spectral radiance) form 120 nm to the corresponding wavelength.

We have ventured to analyze the magnitude of "equilibrium" radiance by integrating over defined spectral regions and studying velocity and pressure dependencies. Examples of such analyses are shown in Figure 22. The data generally display strong velocity dependence. Pressure scaling, on the other hand, is nearly linear. Power law analyses of the velocity trend extract exponents between 8 and 20, depending on spectral region. However, a power law dependence is not the most accurate representation of the trend, and other functional forms have been used, such as $Ap^n exp(-E/v^2)$ (Arrhenius-like, shown in Figure 22) or modified Arrhenius and Hill expressions.[4] In the regions of significant radiance, a linear relationship (with a non-zero intercept) could even be applied. For the case of CO_2/N_2 radiation, a single fit of this form fails as the radiation transitions from being primarily molecular to primarily atomic above 10 km/s. The fit shown in Figure 22(a) consists of the sum of two Arrhenius-like equations. While these correlations may be useful for basic analysis, there is no real substitute for performing a full radiative simulation, which will take into account the complex dependencies on species densities, temperatures and radiative pathlength. Codes used for these purposes at NASA include HARA and NEQAIR.
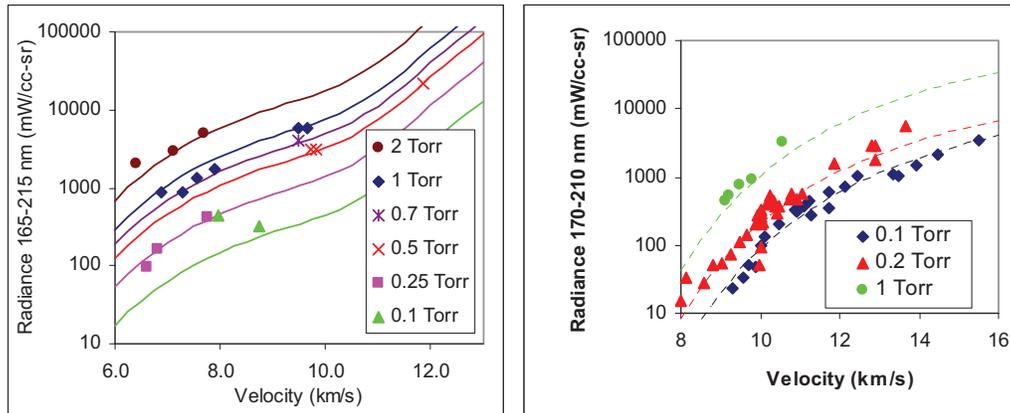
Figure 22. Measurements of radiance versus velocity for (a) CO_2/N_2 and (b) Air. The lines on the plots are parameterized fits

Measurements in the mid-infrared have shown potentially significant radiative heating from CO_2 molecules at relatively low temperatures. An example of such data, and the associated radiative magnitude versus velocity is shown in Figure 23. In this case, the heating trend is opposite that observed at lower wavelength, in that it is decreasing with velocity over a majority of the range measured. This is due to the dissociation of CO_2 occurring as velocity increases. At around 6 km/s, the CO_2 is almost completely dissociated and the remaining radiation is attributable to CO. The CO radiance does increase further as velocity is increased. It is expected that measurement at lower velocity would reveal the radiance observed at 3 km/s to be a maximum for the EAST geometry. This observation has interesting implications for low speed entries and backshell heating in Martian entry, and will merit consideration in future heat shield sizing. In fact, the recent measurements made during the Mars Science Laboratory entry in 2012 showed a 15 W/cm^2 underprediction of heat flux[13, 14] that could be attributed to this mechanism.
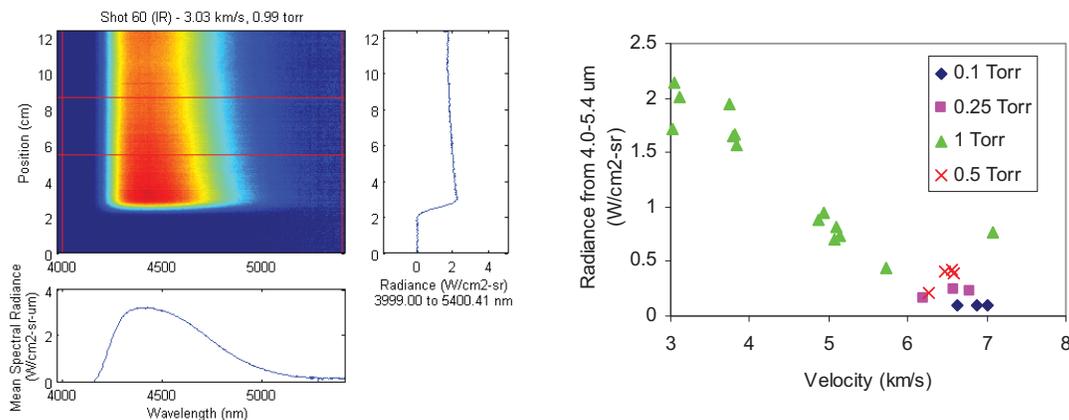
Figure 23. (a) Measurement of Mid-wave infrared radiation for a low velocity CO_2 shock. (b) MWIR radiance versus shock velocity.

In air testing, we have used lineshapes to deduce electron densities in the shock wave. This has been attempted using several different lines present in the air spectrum. Trace amounts of hydrogen present in the experiment

have produced hydrogen Balmer-α (656 nm) and β (486 nm) lines, both of which have well characterized Stark widths. Additionally, Stark broadening data exists for the 410 and 411 nm lines of nitrogen, which has been used to extract number density. The measurement of some of these lines is shown in Figure 24(a). An electron density is obtained by convolving the Instrument Line Shape (Sect. 2.1.1) with a Lorentzian function that describes the actual lineshape. In the case of H-β, a more complicated lineshape is required. The fit then consists of a single adjustable parameter which is proportional to the electron density by a power law relation (i.e. $\Delta\lambda = An_e^\alpha$, $\alpha = 1$ for N and 3/2 for H). The result of this analysis over several conditions is shown in Figure 24(b). Also shown are the equilibrium levels predicted by CEA (Chemical Equilibrium with Applications) code. It can be seen that the EAST tests follow equilibrium fairly well at high velocity, but begin to diverge at lower velocity. Possible reasons for this divergence will be discussed in the next section.
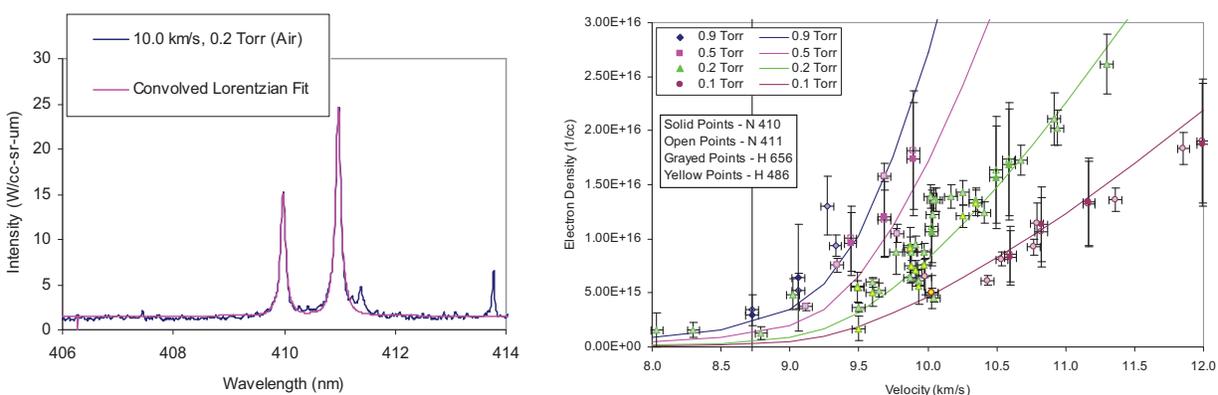
Figure 24. Electron density measurements in air shocks via Stark Broadening. (a) Shows the fitting of two line with a Lorentzian convolved with the instrument lineshape, (b) shows the results of several different tests. The color and shading of the symbols denote different pressure conditions, while the shading identifies which line is used for the fit. Solid lines are the expected equilibrium electron densities.

In Mars testing, the molecular bands present provide opportunity for obtaining temperature data within the shock. For optically thin molecular bands, such as the CN Violet band, the band shape is a function of both rotational and vibrational temperature. With knowledge of the instrument lineshape, a computed band may be convolved by the lineshape to produce a synthetic spectrum, which may then be subjected to a non-linear optimization to obtain vibrational and rotational temperatures. The result of such an analysis is shown in Figure 25(a). For optically thick bands, such as the CO 4th Positive in the VUV and the CO_2 vibrational in the mid-infrared, the band may be compared to the Planck function to obtain an estimated blackbody temperature measurement in the shock (Figure 25(b)). The temperature extracted by this method depends on the nature of the band - for an electronic excitation, it will be the electronic temperature, for a vibrational excitation, it will yield vibrational temperature. These temperature measurements are compared against shock velocity in Figure 25(c,d). In general, the trend follows the equilibrium temperature line, but are generally higher than equilibrium.
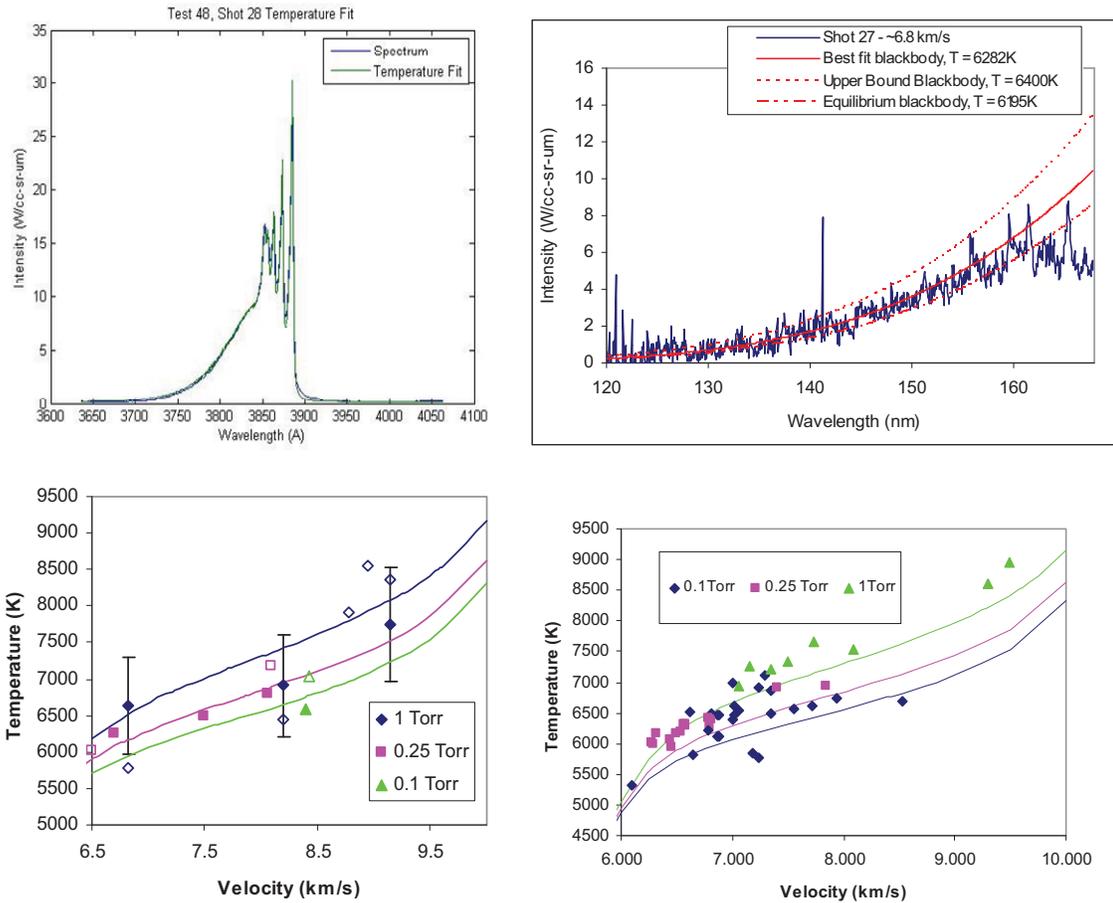
Figure 25. Temperature Measurements for CO2/N2 entries. (a) CN spectra with corresponding band fit, (b) Blackbody-limited portion of CO 4th Positive radiation with Planck curve fit. (c) Extracted rotational temperature versus velocity over pressure. Solid symbols are from fits of CN, while open symbols originate from C_2. (d) Extracted electronic temperature versus velocity. The solid lines in (c) and (d) represent the corresponding equilibrium temperatures.

3.2. Spatial Analysis

Cross sections in the vertical direction, integrated over a particular region, are used to obtain information regarding the shock relaxation. The spatial trends for selected air entries are shown in Figure 26. The figure includes relaxation data obtained at 8, 10 and 12 km/s at 0.2 Torr. The spectral range integrated corresponds the Vis/NIR camera and spans from 480 to 900 nm. Radiation in this region is mostly attributable to atomic lines of N and O, although there is some continuum region underlying this radiation which is primarily bound-free excitation. The shock front is identified from the onset of radiation : this does not mark the "true" shock front, as any kinetic induction time is not accounted for. The images have been shifted slightly to align this onset to the same location. In the 3D spectra, the contact front is often identifiable by the appearance of contamination lines; in the 2D traces below the contact front is identified by a sudden change in slope of the curve. At the lowest velocity of 8 km/s, the radiance shows a non-equilibrium overshoot within the first cm, followed by a relaxation to a steady state level a few cm behind the shock. Some slight increase in radiance is apparent within this

nominally steady region before the contact front transition appears. At 10 km/s, the non-equilibrium overshoot is much smaller. A secondary rise follows the initial non-equilibrium and never settles into a steady radiance. Early attempts at understanding the EAST data followed this rise to the far end of the camera in order to locate the equilibrium radiance, however our current understanding is that this curve is diverging from equilibrium. Finally, at 12 km/s, the radiance rises to a steady level with no overshoot. The somewhat slower rise as compared to slower speeds is attributed to the spatial resolution function's dependence on velocity [Eq. (2.5)]. The radiance holds a steady level for several cm before it begins to decrease. The decrease in radiance has been tentatively attributed to the non-adiabatic affect, i.e. the radiance is so large as to cause the flow to lose energy as it gets further away from the shock front. Other plausible explanations for this trend, such as a trailing expansion wave or boundary layer growth, would require further confirmation. Also noteworthy on this figure are the levels of radiance. The peak radiance has increased 20-fold in going from 8 to 12 km/s, though the steady level of radiance has changed another order of magnitude beyond on that (similar to the VUV velocity trend in Figure 22).
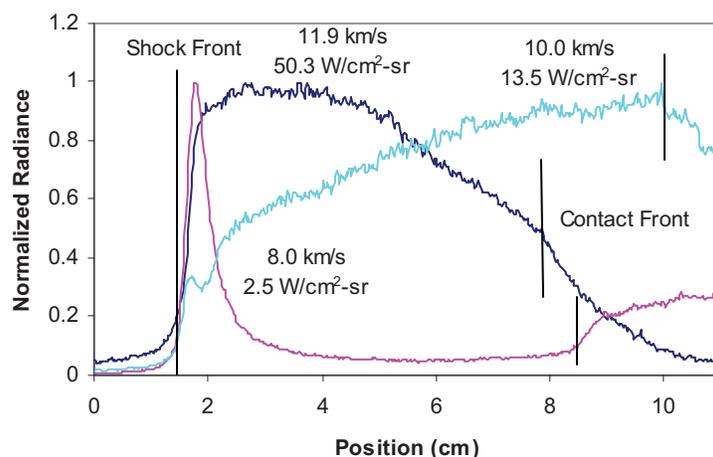
Figure 26. Spatial traces of normalized radiance for air entries from 480 to 900 nm. The text labels show the peak intensity (normalization factor) applied to each trace. Freestream pressure was 0.2 Torr. The approximate locations of shock and contact front are marked.

The trends in radiance versus position may be better understood through examining the trends in electron density versus position. By taking the Stark analysis discussed in the previous section, and applying it to different rows in the camera, it is possible to obtain the electron density trend behind the shock as well. This is shown in Figure 27 for three different conditions in air at 0.2 Torr. As the currently available Stark broadening measurements do not cover the same range as the radiance measurements, the range examined is somewhat more narrow - the figure contains electron density trends at 9.6, 10.0 and 10.9 km/s. The predicted equilibrium electron densities are shown as dotted lines. The rise in electron density is mostly monotonic, though trends in the non-equilibrium region may be obscured by the relatively long (1 μs) gating time of the camera. At the highest velocity, the plateau in radiance seen in Figure 26 is also apparent in the electron density and is somewhat lower than equilibrium. At 10 km/s, the electron density trend is relatively flat and slightly above equilibrium. At 9.6 km/s, however, the electron density is increasing monotonically from the shock front. A trend of this signal, shown by the heavy solid line, indicates that the equilibrium density is met nearly right at the shock front. A similar evaluation of the 10.0 km/s curve reveals a slight trend, mostly obscured by the noise, which would bring the

density in equilibrium near the shock front. This suggests that the equilibrium calculation is obtaining the correct flow enthalpy at the shock front, where it is most valid, but that the enthalpy is diverging behind the shock front. Reasons for this will be discussed below.
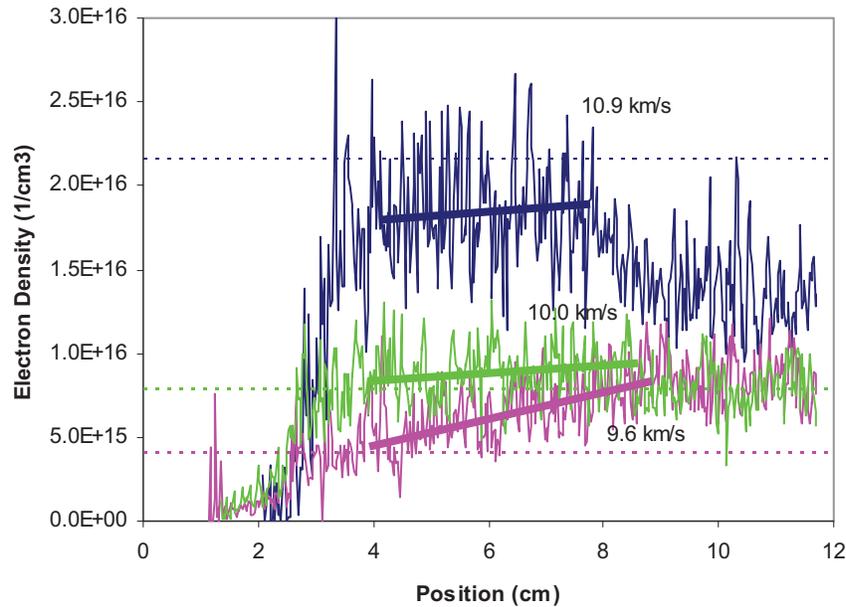
Figure 27. Temporal electron density trend in air at 0.2 Torr. Dotted lines show the expected equilibrium level and heavy solid lines show the linear trend within the test time.

Studies of spatially resolved radiance data in the EAST have been used to understand the kinetics (reaction rates) in Martian gas. An example of such analysis is shown in Figure 28, where the radiance has been integrated from 333-496 nm (CN Violet radiation) to observe the trends in radiation from CN. This particular data set shows a two-step decay at 6.5 km/s (nominal), 0.25 Torr, and a more gradual rise followed by single decay at 7.0 km/s (nominal), 0.1 Torr. The trend in the first case is attributed to the initial decay in shock temperature followed by the decomposition of CN. In the absence of N_2 in the mixture, the secondary decay is not observed and only the trend attributed to temperature is apparent. Interestingly, the $CO_2/N_2/Ar$ and CO_2/N_2 mixtures both show nearly the same level of radiance at the end of the temperature decay portion, in spite of having more than a 2x difference in N_2 mole fraction. This suggests the kinetics of CN formation may be independent of N_2 fraction. This would be the case were the following reactions brought to equilibrium:

$$N_2 + M \rightleftharpoons 2N + M$$
$$N_2 + C \rightleftharpoons CN + N$$

$$(3.1)$$

in which case the CN concentration would be only a function of the equilibrium constants and C concentration. The C concentration would be controlled by CO dissociation which is not strongly dependent on N fraction (see below). In the lower pressure case, the curves can be shown to overlay exactly when normalized to their peak value. This is suggestive of a first order process for both CN formation and destruction. This would suggest the

following reaction:

$$CO + N \leftrightarrow CN + O \tag{3.2}$$

is controlling the CN concentration. In this case the CN density is proportional to the N atom density, equilibrium constants and [CO]/[O] ratio. The N atom may be expected to scale with N_2 fraction in the mixture, while the other parameters will be roughly independent of N_2 fraction.
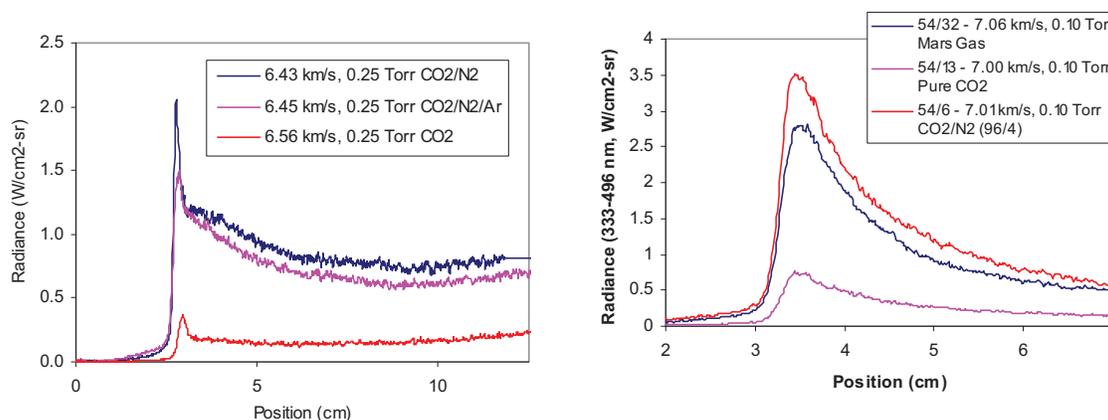
Figure 28. CN Relaxation trends in different Martian mixtures

The radiance measured reflects the density of the excited molecular states and to first approximation is directly proportional to their density. However, absorption by the molecular ground also affects the magnitude, particularly for CO. In order to understand the data then, it is necessary to perform first the CFD calculation to obtain density and temperature profiles, an internal excitation/de-excitation (i.e. non-Boltzmann, QSS) calculation to obtain excited species densities, a volumetric radiation calculation to obtain emission and absorption coefficients and a radiative transport calculation to obtain the radiative magnitude observed in experiment. Typically, the first step would be performed in a CFD solver while the final three are done within the radiation code. However, some efforts have been made to combine all of these into a single code.[15] Finally, the result must be convolved with the spatial resolution function to account for the experimental resolution limits. The result is sensitive to all of these steps. The spatial resolution functions are now relatively well understood as discussed in Sect. 2.1.2. The radiative transport and volumetric radiation calculations may be validated through equilibrium analysis (Sect. 3.1), leaving only the CFD and internal reaction kinetics to be solved to match the profiles. The latter effect may be minimized by limiting studies to higher pressures where the QSS equations equilibrate more rapidly.

EAST data has been analyzed for kinetic rates via a relaxation time analysis. This involves fitting the experimental and predicted decay functions with one or more exponentials and comparing the two. In a recent study, we have taken the electronic temperature trend (see below and Sect 3.1) and identified two distinct relaxation rates as shown in Figure 29(a). The first decay rate is attributed to the energy lost in CO_2 dissociation, while the second is assigned to CO dissociation processes. Analysis of the slower rate in terms of relaxation times are given in Figure 29(c). The solid and dashed lines show how these rates have led to adjustments in CO kinetic rates in order to better match the data. In particular, a mechanism causing CO dissociation via the

following compound reaction:

$$CO + N \rightleftarrows NO + C \xrightarrow{M} N + O + C \qquad (3.3)$$

was re-evalutated in light of the lack of N density dependence on the temperature relaxation. This rate was made less significant by using reliable literature sources.[16] However, the rate of decomposition via the primary reaction:

$$CO + M \leftrightarrow C + O + M \qquad (3.4)$$

had to be increased to compensate this change. While an intermediate working chemistry has been obtained, the study is still considered in progress at this stage. With knowledge of the temperature profiles, it is possible to convert the CN decay to a relative concentration profile, as shown in Figure 29(b). This profile in turn has been fit with its own decay time and shown to have reasonable agreement with existing rates [Figure 29(d)].
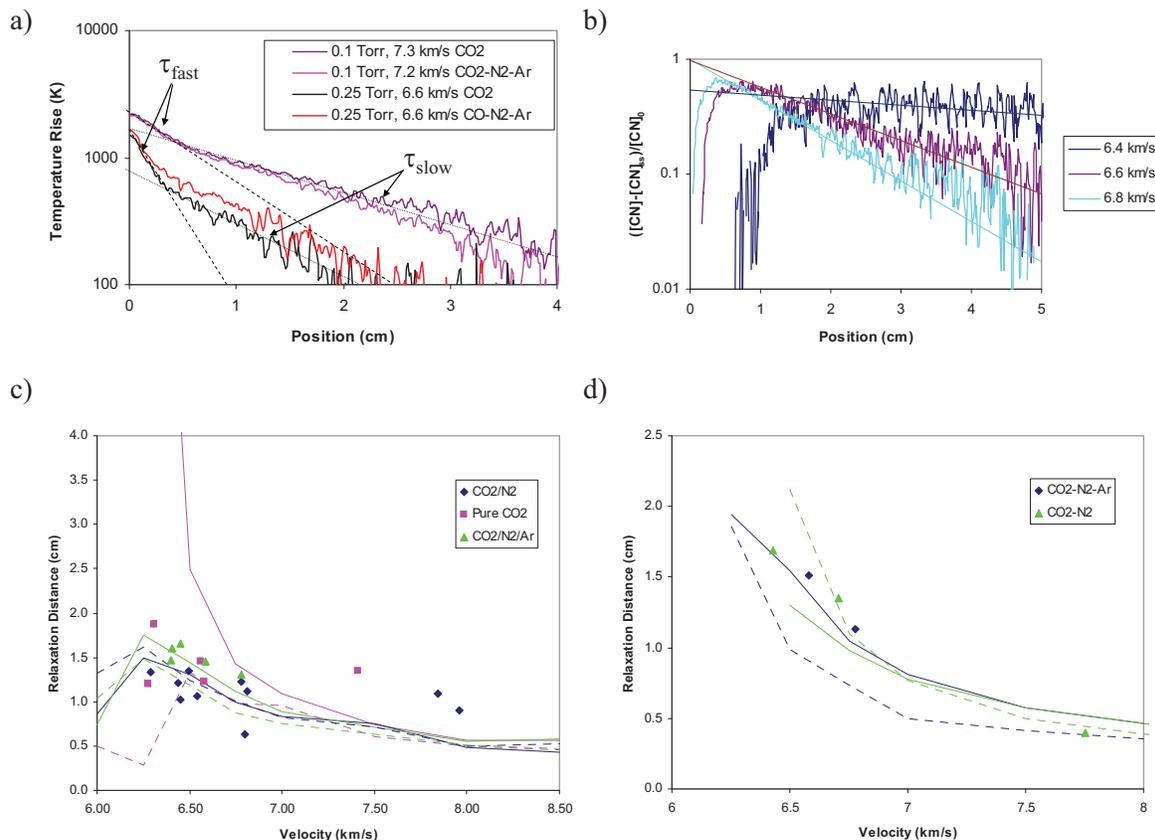
Figure 29. Kinetic Analysis of EAST Data. (a) Shows the Temperature decay on a logarithmic plot, (b) shows the CN radiance, normalized and with Boltzmann factor removed. Both plots yield exponential decays which are shown in figs (c) and (d) over a range of conditions studied. The solid and dashed lines are from the baseline and adjusted chemistries.

In addition to the relaxation time analysis, the approaches to temperature measurement detailed in Sect. 3.1 have been applied to separate pixel rows to obtain temperature as a function of position in the shock. The rovibrational relaxation obtained from CN is shown in Figure 30(a). The fits do not contain spatial resolution function corrections and the quality of the fit is suspect in the pre-shock region where the radiance level is low, but should be relatively good in the decay region of the spectrum. Also shown on the plot is the CFD prediction for relaxation on a blunt body stagnation line. The fit is fairly well matched beginning with the peak vibrational temperature predicted by CFD. The larger peak vibrational temperature in the experimental fits is most likely an issue with the quality of the fit rather than an indication of an underprediction by CFD. This trend of electronic temperature beyond the shock front, and the comparison to equilibrium, is shown in Figure 30(b). Here, the peak temperature is blunted by the relatively long (1 μs) exposure time of the camera and the decay never reaches the equilibrium level of radiance. The temperature deduced by this method in fact is diverging from equilibrium as distance behind the shock front increases. Qualitatively similar observations were made in the analysis of air entries in terms of both radiance levels and electron number density.
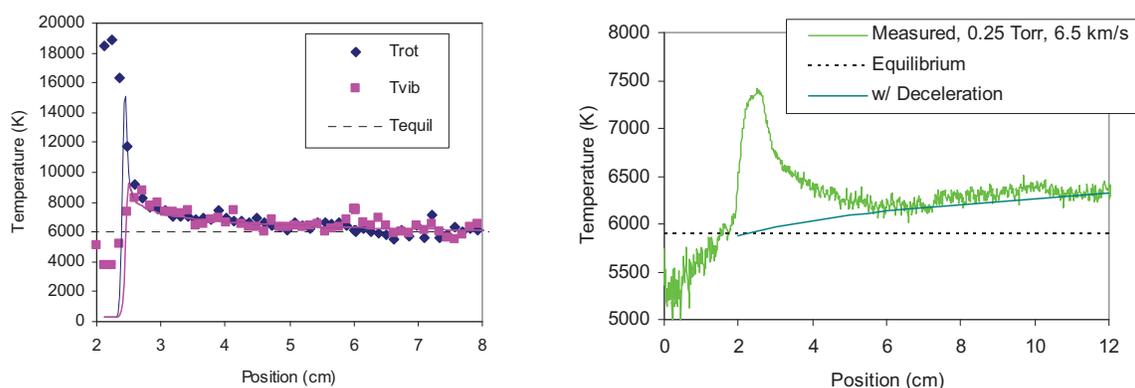
Figure 30. Temperature relaxation trends behind the shock as deduced by (a) CN robvibrational temperature fits at 6.9 km/s and 0.1 Torr and (b) Blackbody radiation limit in the VUV at 6.5 km/s and 0.25 Torr. In both plots, the dotted lines show the expected equilibrium radiance. In (a), the solid lines show a prediction for a blunt body stagnation line relaxation via CFD. In (b), the solid line is originates from the shock deceleration model discussed in the text.

We have here demonstrated, by two different methods and for two different chemistries, a divergence from equilibrium behind the shock front. In one case, the divergence is associated with an increasing electron density, in the other an increasing electronic temperature. Both cases are suggestive of related mechanisms and ultimately imply that the shock enthalpy is increasing behind the shock front. This is counter to the assumption of *similarity*, whereby the freestream pressure and shock velocity is thought to produce the same characteristic as the blunt body stagnation line in free flight. The phenomenon may be better understood by examining the x-t diagram, an idealization of which is shown in Figure 31. The x-t diagram for EAST is relatively straightforward. Ideally, the primary shock is followed by the contact front, which defines the test time. However, the presence of an expansion wave reflected off the back of the driver (which is relatively shallow) cannot be discounted. For certain conditions, this may interfere with measurements and further analysis would be required to determine when or if this will be an issue. If the wave were carrying contamination with it, it would typically be excluded from the analysis, but may be limiting the test time. Another phenomenon, not depicted in Figure 31, is the presence of secondary shocks due to the ringing characteristic of the arc driver. These tend to occur at high

driver voltages and are obvious in the spectra when they occur. When the secondary shock is cleanly separated from the primary shock, it marks the end of the test time. Often this phenomenon is associated with contamination throughout the test, and would account for some of the shocks that are not considered "good" in Table I.
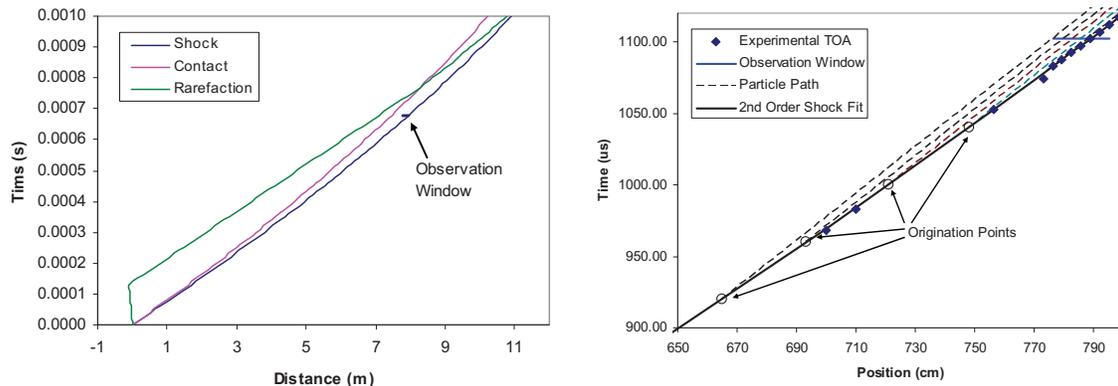
Figure 31. Estimated x-t diagrams for the EAST facility. (a) Shows the primary shock, contact and reflected expansion waves, (b) shows the close-up in the test section region with actual experimental data. The dotted lines trace the fluid velocities from their point of origination to where they are observed in the imaging experiment.

The present discussion will focus around the deceleration of the shock wave. Measurements of time of arrival versus position clearly demonstrate that the shock decelerates by as much as 30% from the driver to the test section. This is apparent as an upward curvature on the x-t shock trace in Figure 31(a). This deceleration is typically attributed to viscous effect (i.e. boundary layer drag), though loss of energy in the driven gas as it expands may also play some role. A close up of the test section region is shown in Figure 31(b), where the shock curve is here given as a fit to the actual data. The dotted lines in Figure 31(b) display the fluid displacement originating upstream, assuming a constant fluid velocity. Observation at the test section, marked by the horizontal line, will then show the characteristic of the fluid that originated upstream, where the shock velocity is higher. Supposing the dotted lines to be adiabatic, the enthalpy will be higher behind the shock than the instantaneous shock velocity suggests. As a simplistic approximation to the temperature trend, this enthalpy difference has been computed and divided by the heat capacity to obtain a temperature profile as shown in Figure 30(b). The agreement of this profile is encouraging, but more detailed simulation is required to confirm the mechanism.

Earlier attempts to study the impact of deceleration on EAST data showed that the ratio of continuum to line radiation could be matched reasonably well.[17] This is consistent with the ionization fraction and electron density, but not neutral densities and temperatures, being elevated by this mechanism. The increased ion density could be attributed to an increase in electron temperature. This may be considered consistent with the higher electronic temperature observed in the VUV radiation from CO. The result suggests that proper analysis of the EAST data would require a separate electron temperature equation, which is tracked from the origination point of the fluid volume. The data appears to indicate that, for whatever reason, the electron temperature will not relax to the equilibrium level as the neutral temperature does.

4.0 CONCLUSIONS

The EAST facility, since 2008, has been a prolific source for radiation validation data. Presently, over 1300 images are available for analysis of spectral radiance as a function of wavelength and position for shock waves traveling at velocities from 3-15 km/s and freestream pressures from 0.01-2.0 Torr, in gas mixtures representative of Earth, Martian and Venutian entry environments. These images are publically available and may be obtained by contacting the author. This paper has detailed the specifics of the facility and data collection. Particular attention has been paid toward describing calibration approaches and the resolution limits of the data. In order to correctly analyze the data, it is necessary to apply convolution functions in both the spectral and spatial dimensions:

$$I_{meas}(\lambda, y) = \left[I_{true}(\lambda, y) \otimes ILS(\Delta\lambda) \right] \otimes SRF(\Delta y) \tag{4.1}$$

The methodology for obtaining the resolution functions are discussed in Sections 2.1.1 and 2.1.2, and the results of such analyses have been tabulated by the author and are provided with the data releases. However, we continually strive to improve the quality of this characterization and thus expect there to be updates in the future.

A summary of data collected for Mars and Earth data to date has been presented. Data has been analyzed in terms of a nominal equilibrium spectral radiance and a spatiotemporal relaxation of certain radiating regions. The equilibrium radiance is shown to depend strongly on velocity, and could be characterized as a power law of greater than the 8th power, but is better represented by an exponential or Arrhenius type scaling. Different scaling regimes exist as the radiance transitions from molecular to atomic dominated. At low velocity, in Mars entries, a significant radiative signature from CO_2 vibrational modes is observed in the mid-infrared. This signature maximizes at relatively low velocities ($\sim$ 3 km/s) so could produce a secondary heat pulse for some entry scenarios. In other cases, such as MSL, it has likely contributed a heating magnitude which was not anticipated due to the low velocity.

For Martian entries, the radiance magnitude has been analyzed as a function of position to extract kinetic data. The Martian entry is generally in a regime where changes to the kinetic model can have significant impact on convective heating,[18] so this source of validation and tuning data is invaluable. We have made qualitative understandings of the shock kinetics through comparison of trends at different N_2 loadings. Quantitative analysis through relaxation time extraction has led to tuning of the kinetic models to better fit the data. More work in this area is still required.

Air entries have been analyzed for electron density via Stark broadening measurements on trace amounts of hydrogen and some of the broader N lines present. The characterization has shown a generally higher than equilibrium electron density at low velocity, but at higher velocity the density becomes more consistent or even lower. This trend is somewhat better understood by examination of the temporal trends in radiance and electron density. Often, a large electron density is associated with a radiation and density trend that is monotonically increasing away from the shock front. Extrapolation of the data back to the shock front shows equilibrium to be matched near the shock front where the Rankine-Hugoniot solution is most valid. At higher velocities, a plateau region is typically observed that is relatively consistent with equilibrium. A decay following the plateau may be at least partially explained through radiative cooling/non-adiabatic effects that can be captured by a coupled flow and radiation solver. However, the possibility that this decrease marks the expansion wave reflected off the back of the driver cannot be discounted.

Temperature trends extracted from the Martian data show similar discrepancies. While the rovibrational analysis from CN bands show a decay to equilibrium that is well matched by the CFD models, the analysis of electronic

temperature via the Planck-limited vacuum ultraviolet region indicates the temperature to be diverging from equilibrium behind the shock. A divergence of electron temperature behind the shock front would be consistent with an increasing ionization fraction, as observed in air entries. Initial attempts to understand this divergence have pointed to analyzing the shock wave characteristics as the relaxation of fluid elements from their upstream point of origination rather than assuming similarity to a blunt body stagnation line characterized by the instantaneous shock velocity. Preliminary analyses show this to be consistent with both temperature and ionization data. Further understanding of this requires development of time accurate facility models. The discrepancy from electronic and rovibrational temperature suggests the need for separate electron energy equations in said model.

APPENDIX A. EVALUATION OF THE SPATIAL OPTICAL RESOLUTION FUNCTION

In order to evaluate the optical function, we consider that each x value on the spectrometer represents the light collected by a cone passing through the tube at some off-normal angle θ_0, as shown in Figure A1. This angle defines the *principal ray*, which lies in the x-y plane. The cone is defined by a half-angle ϕ_m, with rays on the outer surface of the cone being *edge rays*. The power collected through this cone is given as:

$$I = \iint_S i_{\varphi\theta} \cos\psi \, dS \tag{A.1}$$

where S is the area defined by the intersection of this cone with the window at the wall of the tube, shown as a dashed elliptical shape in Figure A1, and ψ is the angle off normal at this intersection. The radiance $i_{\theta\phi}$ is the line integral of the volumetric radiance along the line of sight defined by angles ϕ and θ. The angles ϕ and θ follow the normal definition of spherical co-ordinates where θ is the projected angle in the x-y plane and ϕ is the angle in the z-direction off of this projection. Under an optically thin assumption, for any ray within the cone, the radiance is given by:

$$i_{\varphi\theta} = \int_{-r_m}^{r_m} E(x) \, dr \tag{A.2}$$

Where E is the volumetric radiance and is assumed to be a function of x only. The bounds r_m are the lengths of the rays that intersect with the window at y = R. In order to evaluate this integral, it is convenient to change the radial co-ordinate to an axial co-ordinate. This is done by using $x = r\cos\varphi\sin\theta$ and $R = r_m \cos\varphi\cos\theta$, then substituting into the equation:

$$i_{\varphi\theta} = \int_{-R\tan\theta}^{R\tan\theta} \frac{E(x)}{\sin\theta\cos\phi} \, dx \tag{A.3}$$

Alternatively, if one were to consider the radiance as optically thick, this relation would simply be:

$$i_{\varphi\theta} = I(x) = I(R\tan\theta) \tag{A.4}$$

where I(x) is the optically thick radiance at position x.
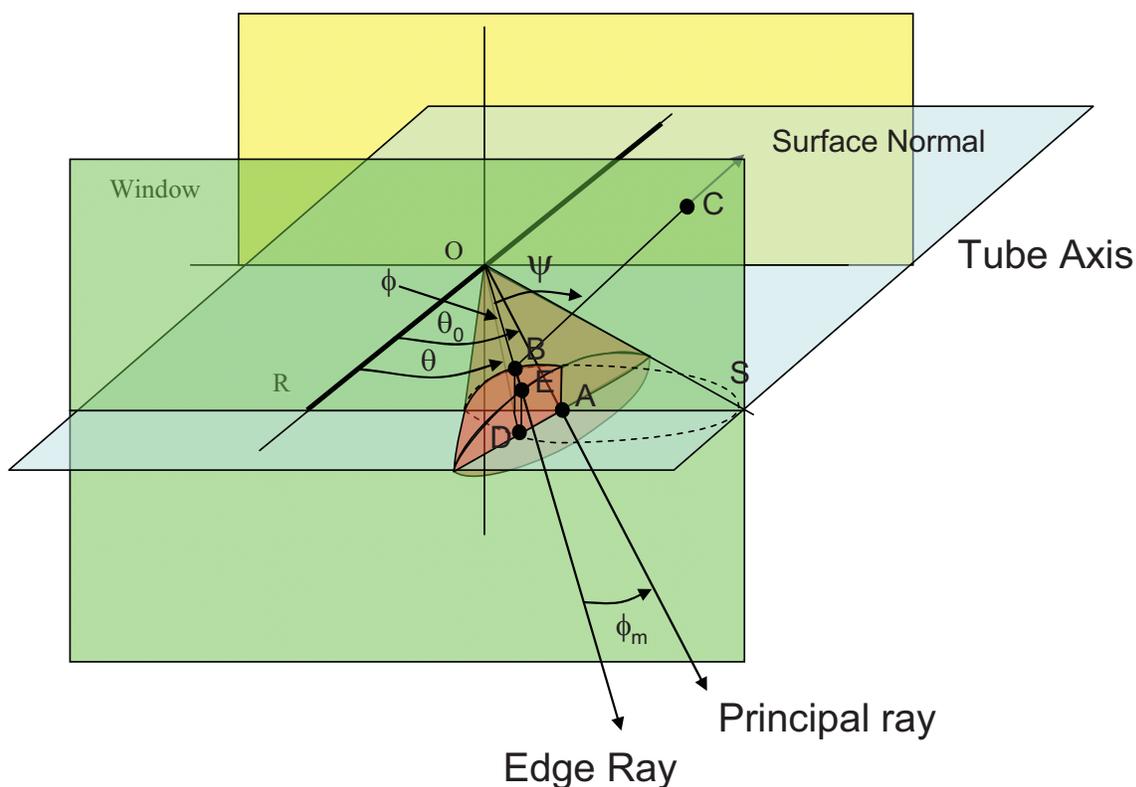
Figure A1. Three dimensional sketch of optical collection volume

Next, we evaluate the off-normal angle, ψ. From Figure A1, ψ is the angle formed from segment OB to the surface normal emanating from B. A right triangle OBC is formed by taking the intersection of this triangle with the x-z plane and the angle is found as:

$$\cos\psi = \frac{BC}{OB} = \frac{R}{R \big/ \cos\theta\cos\phi} = \cos\theta\cos\phi \tag{A.5}$$

Second, the surface projection must be obtained. The differential surface area dS, is found from:

$$dS = dxdz = d\left(R\tan\theta\right)d\left(\frac{R\tan\phi}{\cos\theta}\right)$$

$$dS = dxdz = \frac{R^2 d\theta d\phi}{\cos^3\theta\cos^2\phi} \tag{A.6}$$

Next the limits of integration must be discerned. θ spans from $\theta_0 \pm \phi_m$. The limits on ϕ are determined by the angle formed by the edge ray, call it ϕ_e. In order to determine how this angle depends on θ, we consider the three right triangles connecting points O, A, D and E:

$$\cos\phi_e = \frac{OD}{OE}$$

$$\cos\phi_m = \frac{OA}{OE}$$

$$\cos(\theta_0 - \theta) = \frac{OA}{OD}$$

(A.7)

And therefore:

$$\cos\phi_e = \frac{\cos\phi_m}{\cos(\theta_0 - \theta)}$$

(A.8)

Combining these together, we return to equation (A.1):

$$I = \iint_S i_{\varphi\theta}\cos\psi\, dS = \int_{\theta_0-\phi_m}^{\theta_0+\phi_m}\int_{-\phi_e}^{\phi_e}\int_{-R\tan\theta}^{R\tan\theta} E(x)dx \frac{R^2 d\phi d\theta}{\cos^2\phi\sin\theta\cos^2\theta}$$

(A.9)

The integral in ϕ can be integrated independently:

$$I = \int_{\theta_0-\phi_m}^{\theta_0+\phi_m}\int_{-R\tan\theta}^{R\tan\theta} E(x)dx \frac{2\tan\phi_e R^2 d\theta}{\sin\theta\cos^2\theta}$$

(A.10)

with

$$\tan\phi_e = \sqrt{\frac{\cos^2(\theta_0-\theta)}{\cos^2\phi_m} - 1}$$

(A.11)

For the optically thick case, the equation reduces to:

$$I = \iint_S i_{\varphi\theta}\cos\psi\, dS = \int_{\theta_0-\phi_m}^{\theta_0+\phi_m}\int_{-\phi_e}^{\phi_e} \frac{I(R\tan\theta)R^2 d\theta d\phi}{\cos^2\theta\cos\phi}$$

(A.12)

The ϕ dependence can be integrated to obtain:

$$I = \int_{\theta_0-\phi_m}^{\theta_0+\phi_m} \frac{I(R\tan\theta)R^2}{\cos^2\theta}\ln\left(\frac{1+\sin\phi_e}{1-\sin\phi_e}\right)d\theta$$

(A.13)

At this point, we return to the definition of the spatial resolution function:

$$I_{meas}(x) = \int_{-\infty}^{\infty} SRF_{opt}(\Delta x)I(x+\Delta x)d\Delta x$$

(A.14)

We can shift the x-origin in this equation, without loss of generality, and evaluate at x = 0. This will be equivalent to radiance collected as derived in equations (A.10) and (A.13). For the optically thin case, I(x) =

2RE(x):

$$I_{meas} = 2R \int_{-\infty}^{\infty} SRF_{opt}(\Delta x) E(\Delta x) d\Delta x = \int_{\theta_0 - \phi_m}^{\theta_0 + \phi_m} \int_{-R\tan\theta}^{R\tan\theta} E(x) dx \frac{2\tan\phi_e R^2 d\theta}{\sin\theta \cos^2\theta}$$ (A.15)

And for the optically thick case:

$$I_{meas} = \int_{-\infty}^{\infty} SRF_{opt}(\Delta x) I(\Delta x) d\Delta x = \int_{\theta_0 - \phi_m}^{\theta_0 + \phi_m} \frac{I(R\tan\theta)R^2}{\cos^2\theta} \ln\left(\frac{1+\sin\phi_e}{1-\sin\phi_e}\right) d\theta$$ (A.16)

Since these equations are to hold for any form of the functions E(x), I(x), these terms may be replaced with delta functions to obtain the form of the optical SRF:

$$SRF_{thin}(\Delta x) = \int_{\theta_0 - \phi_m}^{\theta_0 + \phi_m} \int_{-R\tan\theta}^{R\tan\theta} \delta(x - \Delta x) dx \frac{\tan\phi_e R d\theta}{\sin\theta \cos^2\theta}$$ (A.17)

$$SRF_{thick}(\Delta x) = \int_{\theta_0 - \phi_m}^{\theta_0 + \phi_m} \frac{\delta(R\tan\theta - \Delta x)R^2}{\cos^2\theta} \ln\left(\frac{1+\sin\phi_e}{1-\sin\phi_e}\right) d\theta$$ (A.18)

Starting with the optically thin form of the SRF, it is convenient to limit the integral to only positive values of θ. Therefore we define the function:

$$g(\theta_m, \Delta x) = \int_{0}^{\theta_m} \int_{-R\tan\theta}^{R\tan\theta} \delta(x - \Delta x) dx \frac{\tan\phi_e R d\theta}{\sin\theta \cos^2\theta}$$ (A.19)

and the thin equation can be written in terms of this function as:

$$SRF_{thin}(\Delta x) = g(\theta_0 + \phi_m, \Delta x) - g(\theta_0 - \phi_m, \Delta x)$$ (A.20)

Evaluation of the function g may be limited to positive values of θ in the integrand by recognizing the function itself is odd-valued. Therefore,

$$g(\theta_m, \Delta x) = \text{sgn}(\theta_m) \int_{0}^{|\theta_m|} \int_{-R\tan\theta}^{R\tan\theta} \delta(x - \Delta x) dx \frac{\tan\phi_e R d\theta}{\sin\theta \cos^2\theta}$$ (A.21)

where sgn(θ_m) signifies the sign (+1, -1) of θ_m. The integral of the delta function is unity for /Δx/ < Rtan θ and zero otherwise. Therefore, the integration bounds can be re-stated such that this term is unity over the range of integration:

$$g\left(\theta_{m},\Delta x\right)=\begin{cases}\text{sgn}(\theta_{m})\displaystyle\int_{\tan^{-1}\left|\frac{\Delta x}{R}\right|}^{|\theta_{m}|}\dfrac{\tan\phi_{e}\,R\,d\theta}{\sin\theta\cos^{2}\theta} & \left|\Delta x\right|<R\left|\tan\theta_{m}\right|\\[20pt] 0 & \left|\Delta x\right|>R\left|\tan\theta_{m}\right|\end{cases}\tag{A.22}$$

Further analytical evaluation of this function is not possible, but it can be integrated numerically. The integrand is singular at $\theta=0$, and the resulting function g is also singular for $\Delta x = 0$. While the singularity cancels in the evaluation of SRF when $\theta_0 > \phi_m$, the SRF is singular at $\Delta x = 0$ when $\theta_0 < \phi_m$. In spite of the singularity, the integral of g is still bounded, so it may still be used in evaluating the convolution.

Turning now to the optically thick spatial resolution function, the delta function may be evaluated to give:

$$SRF_{thick}\left(\Delta x\right)=\begin{cases}\left(R^{2}+\Delta x^{2}\right)\ln\left(\dfrac{1+\sin\phi_{e}}{1-\sin\phi_{e}}\right) & R\tan\left(\theta_{0}-\phi_{m}\right)<\Delta x<R\tan\left(\theta_{0}+\phi_{m}\right)\\[16pt] 0 & otherwise\end{cases}\tag{A.23}$$

with

$$\sin\phi_{e}=\sqrt{1-\dfrac{\cos^{2}\phi_{m}}{\cos^{2}\left(\theta_{0}-\tan^{-1}\left(\dfrac{\Delta x}{R}\right)\right)}}\tag{A.24}$$

Because of the bounds on the non-zero part of the SRF, this functional form is only symmetric about $\Delta x = 0$ when $\theta_0 = 0$. Further, the function may even be zero at $\Delta x = 0$ for $/\theta_0/ > \phi_m$. The implication of this is that the measurement will be shifted from the x-calibration in this scenario. At present, we will neglect this possibility and instead work with the optically thin spatial resolution function.

The numerical evaluation of these functions will be demonstrated using the existing optical parameters in the EAST facility. The values of θ_0 and ϕ_m are determined from the geometric optics shown in Figure 5. Three types of functions are found for the SRF. Figure A2(a) shows the case where $\theta_0 = 0$, and the functional form is given by the function g in equation (A.22). This is the form approximated as triangular in Sect. 2.1.2 and applies to the telecentric optics present on the VUV, UV/VIS and VIS/NIR cameras. Figure A2(b) and (c) describe the case where $\phi_m < \theta_0$ and is obtained as the difference of two g functions. This sum results in a flat-top and is approximated as trapezoidal in Sect 2.1.2. This functional form applies to both the MWIR and NIR optics at the furthest x distance off axis, but with differing widths. A third form of the function, obtained when $0 < /\theta_0/ < \phi_m$ and not shown in Figure A2, is described by the sum of two positive g functions with different limits, and looks qualitatively similar to Figure A2(a), but with a change of slope at the inner limit. This function is obtained with the IR cameras somewhere between the centerline and edge of the image, and is approximated as bi-triangular in Figure 5(d,f).
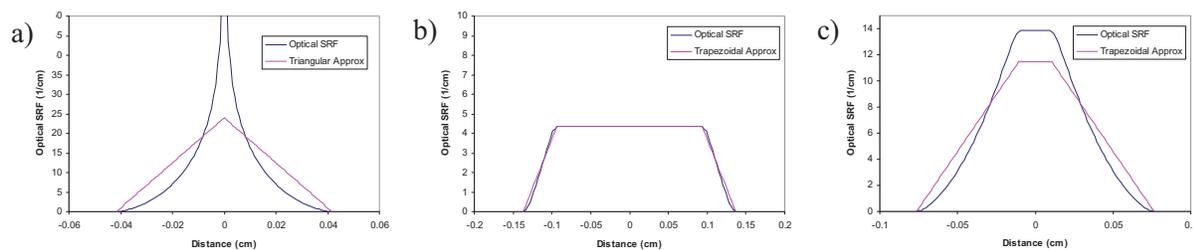
Figure A2. Spatial Resolution Functions on EAST, as calculated from optical design. Also shown are simple approximation functions of the SRF. (a) VUV, UV/Vis and VIS/NIR cameras, (b) NIR camera, (c) MWIR camera.

REFERENCES

[1]   Cruden, B. A., "Radiance Measurement for Low Density Mars Entry," *43rd AIAA Thermophysics Conference*. New Orleans, LA, 2012.

[2]   Cruden, B. A., Martinez, R., Grinstead, J. H., and Olejniczak, J., "Simultaneous Vacuum Ultraviolet through Near IR Absolute Radiation Measurement with Spatiotemporal Resolution in an Electric Arc Shock Tube," *41st AIAA Thermophysics Conference*. AIAA, San Antonio, TX, 2009, pp. AIAA 2009-4240.

[3]   Cruden, B. A., Prabhu, D., and Martinez, R., "Absolute Radiation Measurement in Venus and Mars Entry Conditions," *Journal of Spacecraft and Rockets,* Vol. 49, No. 6, 2012, pp. 1069-1079.

[4]   Brandis, A., Johnston, C., Cruden, B., Prabhu, D., and Bose, D., "Validation of High Speed Earth Atmospheric Entry Radiative Heating from 9.5 to 15.5 km/s " *43rd AIAA Thermophysics Conference*. AIAA, New Orleans, Louisiana, 2012, pp. AIAA-2012-2865

[5]   Brandis, A. M., Cruden, B. A., Prabhu, D., Johnston, C. O., and Bose, D., "Uncertainty Analysis of NEQAIR and HARA Predictions of Air Radiation Measurements Obtained in the EAST Facility," AIAA Paper 2011-3478, June 2011.

[6]   Brandis, A. M., Johnston, C. O., Cruden, B. A., Prabhu, D. K., Wray, A. A., Liu, Y., Schwenke, D. W., and Bose, D., "Validation of CO 4th positive radiation for Mars entry," *Journal of Quantitative Spectroscopy and Radiative Transfer,* Vol. 121, 2013, pp. 91-104.

[7]   Johnston, C., Brandis, A., Panesi, M., and Sutton, K., "Shock Layer Radiation Modeling and Uncertainty for Mars Entry," *43rd AIAA Thermophysics Conference*. New Orleans, Louisiana, 2012, pp. AIAA-2012-2866.

[8]   Bose, D., McCorkle, E., Bogdanoff, D., and Gary A. Allen, J., "Comparisons of Air Radiation Model with Shock Tube Measurements," *47th AIAA Aerospace Sciences*. Vol. 2009-1030, Orlando, Florida, 2009, pp. AIAA 2009-1030.

[9]   Bose, D., McCorkle, E., Thompson, C., Bogdanoff, D., Prabhu, D. K., Gary A. Allen, J., and Grinstead, J., "Analysis and Model Validation of Shock Layer Radiation in Air," *46th AIAA Aerospace Sciences Meeting*. AIAA, Reno, Nevada, 2008, pp. AIAA 2008-1246.

[10]   Bose, D., Wright, M. J., Bogdanoff, D. W., Raiche, G. A., and Allen Jr., G. A., "Modeling and Experimental Assessment of CN Radiation Behind a Strong Shock Wave," *Journal of Thermophysics and Heat Transfer,* Vol. 20, No. 2, 2006, pp. 220–230.

[11]   Grinstead, J. H., Wright, M. J., Bogdanoff, D. W., and Allen, G. A., "Shock Radiation Measurements for Mars Aerocapture Radiative Heating Analysis," *Journal of Thermophysics and Heat Transfer,* Vol. 23, No. 2, 2009, pp. 249-255.

[12] Grinstead, J. H., Wilder, M. C., Olejniczak, J., Bogdanoff, D. W., Allen, G. A., Dang, K., and Forrest, M. J., "Shock-heated Air Radiation Measurements at Lunar Return Conditions," *46th AIAA Aerospace Sciences Meeting*. AIAA, Reno, Nevada, 2008, pp. AIAA 2008-1244.

[13] White, T. R., Mahzari, M., Bose, D., and Santos, J. A., "Post-flight Analysis of Mars Science Laboratory's Entry Aerothermal Environment and Thermal Protection System Response," 2013.

[14] Mahzari, M., White, T. R., Braun, R., and Bose, D., "Inverse Estimation of the Mars Science Laboratory Entry Aerothermal Environment and Thermal Protection System Response," 2013.

[15] Panesi, M., Magin, T., Bourdon, A., Bultel, A., and Chazot, O., "Fire II Flight Experiment Analysis by Means of a Collisional-Radiative Model," *Journal of Thermophysics and Heat Transfer,* Vol. 23, No. 2, 2009, pp. 236-248.

[16] Tsang, W., and Herron, J. T., "Chemical Kinetic Data Base for Propellant Combustion I. Reactions Involving NO, NO2, HNO, HNO2, HCN and N2O," *Journal of Physical and Chemical Reference Data,* Vol. 20, No. 4, 1991, p. 609.

[17] Brandis, A. M., Cruden, B. A., Prabhu, D., Bose, D., McGilvray, M., and Morgan, R. G., "Analysis of Air Radiation Measurements Obtained in the EAST and X2 Shocktube Facilities," *10th AIAA/ASME Joint Thermophysics and Heat Transfer Conference*. Chicago, IL, 2010.

[18] Bose, D., Wright, M. J., and Palmer, G. E., "Uncertainty Analysis of Laminar Aeroheating Predictions for Mars Entries," *Journal of Thermophysics and Heat Transfer,* Vol. 20, No. 4, 2006, pp. 652-662.